Title
Very Low Energy Supernovae And Their Resulting Transients

Author
Lovegrove, Elizabeth Grace

Publication Date
2016

UNIVERSITY OF CALIFORNIA
SANTA CRUZ

VERY LOW ENERGY SUPERNOVAE AND THEIR RESULTING TRANSIENTS

A dissertation submitted in partial satisfaction of the
requirements for the degree of

Doctor of Philosophy

in

ASTRONOMY & ASTROPHYSICS

by

Elizabeth Lovegrove

June 2016

The Dissertation of Elizabeth Lovegrove
is approved:

Professor Stanford E. Woosley, Chair

Professor Daniel Kasen

Professor Brant Robertson

Dr. Weiqun Zhang

Dean Tyrus Miller
Vice Provost and Dean of Graduate Studies

Table of Contents

List of Figures

List of Tables

Abstract

Very Low Energy Supernovae and their Resulting Transients

by

Elizabeth Lovegrove

Core-collapse supernovae play a key role in many of astrophysical processes, but the details of how these explosive events work remain elusive. Many questions about the CCSN explosion mechanism and progenitor stars could be answered by either detecting very-low-energy supernovae (VLE SNe) or alternately placing a tight upper bound on their fraction of the CCSN population. However, VLE SNe are by definition dim events. Many VLE SNe result from the failure of the standard CCSN explosion mechanism, meaning that any observable signature must be created by secondary processes either before or during the collapse. In this dissertation I examine alternate means of producing transients in otherwise-failed CCSNe and consider the use of shock breakout flashes to both detect VLE SNe and retrieve progenitor star information. I begin by simulating neutrino-mediated mass loss in CCSNe progenitors to show that a dim, unusual, but still observable transient can be produced. I then simulate shock breakout flashes in VLE SNe for both the purposes of detection as well as extracting information about the exploding star. I discuss particular challenges of modeling shock breakout at low energies and behaviors unique to this regime, in particular the behavior of the spectral temperature. All simulations in this dissertation were done with the CASTRO radiation-hydrodynamic code.

Mom, Dad, & The Woog: Now you have to call me "Doctor."

Invocation of the Muse

Urania, muse of the stars! Nymph to whom the Greeks ascribed
The measure of the heavens, and the sight of heavenly fire!
Hear the voice of one who labors far into the night
To unravel your long dance of gravity and light.
And though you lay your mysteries before our gaze
With old and careless ease, at the closing of each day;
Still you keep your secrets, and watch with smiling eyes,
As we strive amongst ourselves to uncover your design.
O Calliope, muse of works long-sung,
Who limned with fire the verse of ancient tongues!
Smile upon one who brings before you deeds
Poor by comparison, though hasten I to plead
That though I have not raised up Rome nor torn down Troy,
I strove with a hero's heart, and found a hero's joy
And sought a hero's reward, *kleos* or citations be it named
And sacrificed no less. And dare I claim:
That I have sought beyond what any hero can,
That I have held destruction and creation in my hand,
That though they are but ghosts in the machine,
I have kindled fires of which the Greeks could only dream.

Acknowledgments

Stan Woosley, with the generous assistance of George Fuller, paid me actual money to sit and think about space. Stan helped me learn how to think better thoughts about space, and about the world in general. I can't think of anything nicer to do for someone.

Jimmy Fung, Rob Lowrie, and Mack Kenamond at LANL kindly introduced me to both radiation transport and breakfast burritos. I wouldn't have gone to grad school in the first place without the advice and support of Paul Schechter and Rob Simcoe at MIT, and I wouldn't have finished it without Maria Sliwinski helping me out when I e.g. forgot an important form for the fifth time in a row.

Daniel Kasen, Brant Robertson, and Weiqun Zhang are my ideal group of people to judge this work, and also made assembling and interacting with my thesis committee the fastest and most painless part of the entire process; which has, to my knowledge, never happened to anyone planning a quals or defense talk in the history of ever. Seriously, I had more trouble booking the room. So kudos to you.

Thanks to the human beings without whom I would have long ago set everything I own on fire and run away to live in the woods in a house made of books: the Woog, Andrew Ruef, Dr. Alice Jackson, Dr. Tina Dwyer, Sarah Krell, Dr. Thomas Belulovich, Brandon Moore, Alexandra Petri, Abby Pritchard, Kethenn, Shoat, Knight, Chia, genia, pretty much everyone else in CFP, Coco, Ice, Ether, Patho, Zar, Elspeth, Daft, and Niri. Look what you jerks did. I hope you're proud of yourselves.

My fellow grad students without whom I would be confused, cold, and probably stuck at the airport: Dr. Jennifer Burt, Dr. Katie Hamren, Dr. Caroline Morley, Dr. Justin Brown, (soon to be) Dr. Tuguldur Sukhbold, and Dr. Nathan Goldbaum.

The scientists without whom I would likely be baffled and definitely not be graduating: Weiqun Zhang, Ann Almgren, Daniel Kasen, Rob Simcoe, Paul Schecter, Connie Rockosi.

Special “keeping me sane" thanks go to: LoadingReadyRun & the Desert Bus, the PAX Enforcer Corps, Zach Barth, Mojang Studios, Rooster Teeth, Marvel Comics, Eidos Montreal, Wizards of the Coast, the Glitch Mob, Chipzel, JJ Abrams, *Camellia sinensis*, Bioware, and just basically the internet.

Machines: benjamin, taniquetil, rassilon, arklay, raccoon-city, pleiades, hyades, eudora, cenedril, moonlight, pinto, mustang, carver, and edison, for years of faithful service, at least when the power was on.

Cats of my acquaintance: the Mayor, Appointment Cat, Friendly Cat, Poke, Noise, Signal, Merlin, Armani, Ash, Inara, Mimi, Morwen, White Cat, Pants Cat, Marble Cat, Duncan, and Mr. Fitzwilliam Darcy, Gentleman. Owners of the cats of my acquaintance: sorry I keep coming over to pet your cats.[1]

[1] Just kidding, I’m not sorry at all.

Chapter 1

Introduction: The Nature of Very-Low-Energy Supernovae (VLE SNe)

1.1 The Possibility of Failure

In life there always exists the possibility of failure. This principle also holds true for core-collapse supernovae. CCSNe form neutron stars and black holes, disperse stellar nurseries, stir up the interstellar medium, and, most critically, produce nearly all chemical elements heavier than lithium. Accurate data on their behavior, explosion energy, and occurrence rate feed back into many other branches of astronomy. As time-domain astronomy has improved, far more types of supernovae have been discovered than expected. These data prompt a reconsideration of the range of possible transients from core-collapse, and of what is considered the faintest possible supernova.

All stars heavier than 8 $M_\odot$ can eventually undergo core collapse, but there is no guarantee that this collapse will result in an explosion. A CCSN can "fail" if it does not generate an outgoing shock directly from the collapse of the iron core. Failed supernovae represent an aspect of CCSN behavior that is poorly understood; but observing them requires seeing an event that does not happen. How can they be searched for? Fortunately these stars do not always go quietly into the night. Even if the primary explosion fizzles, other physical processes can produce observable signatures either at or before the time of collapse. In the absence of the standard core-collapse mechanism a star can still generate transients that, while dimmer than a CCSN, are nevertheless observable. In this dissertation we simulate transients that can occur even if the primary core-collapse explosion fails and give predictions to guide observational searches. We also model shock breakout, a bright flash emitted at the beginning of the supernova, and evaluate its usefulness as a means to detect dim transients and retrieve data about the original star. These simulations are key in the era of automated surveys; the first analysis pass is done by software, and that software must be told what to look for, so without simulations of these strange transients surveys may misclassify or exclude them.

The survey of Sukhbold *et al.* (2015) found that neutrino-powered supernovae from 9 to 120 $M_\odot$, with central engines calibrated to reproduce the known properties of the Crab supernova and SN 1987A, fell into two categories: failures, which did not blow up at all and made black holes, and robust explosions with energies above 10^{50} erg. While the treatment of neutrino transport was approximate, this behavior suggests a sensitivity to presupernova properties and an explosion mechanism that is "gated," i.e. it either works well or not at all. Achieving a neutrino-powered explosion of $\sim 10^{49}$ erg, for example, would require fine tuning. The term "very-low-energy supernova" (VLE SN) is therefore defined in this work as a transient from a massive, evolved star with a final kinetic energy significantly less than the ~ 0.6 B[1] expected from core collapse, generally less than 0.3 B. Failed CCSNe are the most likely to produce VLE SNe either at or just before the time of death via other processes, and if a VLE SN is detected, it can be attributed with reasonable confidence to a core-collapse failure.

The majority of the hydrodynamic and radiation-hydrodynamic simulations published in this dissertation were run using the CASTRO code. CASTRO (Almgren *et al.*, 2010) is a multi-dimensional Eulerian compressible hydrodynamics code with adaptive-mesh refinement, stellar equations of state, nuclear reaction networks, and self-gravity. It incorporates the multigroup flux-limited diffusion (MGFLD) transport of radiation (Zhang *et al.*, 2013). Further code details will be given in sections as they pertain to the simulations in question. For a full discussion of CASTRO's inner workings, its AMR algorithms, its numerical treatment of radiation, and other specifics, see the code papers Almgren *et al.* (2010), Zhang *et al.* (2011), and Zhang *et al.* (2013). For a discussion of flux-limited diffusion, see Appendix A. CASTRO and its radiation counterpart are both public codes and can be accessed at https://github.com/BoxLib-Codes.

1.2 Constraints on VLE SN Progenitors

It is well-understood that core-collapse supernovae originate in massive, evolved stars that have built up an iron core. This core eventually becomes unstable and collapses into a neutron star, which is both much smaller and much stiffer than the original core. The implosion wave ricochets off this compact object and becomes an explosion wave that blows apart the star. This picture seems simple, but in reality there are many unknowns in the process, particularly concerning the

[1] B stands for "bethe," a unit of energy named in honor of supernova pioneer Hans Bethe. 1 bethe = 10^{51} erg, the final kinetic energy of a "typical" CCSN.

transformation from an implosion to an explosion. Simulations of this transition have produced mixed results and it is unclear not only how it proceeds, but also whether it consistently happens at all. There exist constraints from both observation and theory on which mass ranges of progenitor stars must explode with a certain frequency, but these constraints leave substantial room for certain stars to fail to explode in some or even all cases.

1.2.1 Constraints from Observations

Though the existing sample of observed CCSNe progenitor stars is small, by now it shows a clear and statistically significant trend: all recovered progenitors are smaller than 20 $M_{\odot}$ (Smartt, 2015). This suggests that either high-mass progenitors are preferentially obscured, or they are more likely to collapse in a non-traditional way. Wide-field supernova surveys at a range of redshifts can compare the observed supernova rate (SNR) with the observed star formation rate (SFR). If 100% of stars capable of forming a CCSN did so, the SNR would equal the fraction of the SFR at or above 8 $M_{\odot}$.[2] Current data suggest that the SNR may fall below the SFR by as much as 30% (Horiuchi *et al.*, 2011). Some of these missing supernovae can be attributed to dust obscuration, survey biases, etc. but these systematics cannot make up the difference. Fewer stars are exploding than we would expect from a model in which every CCSN succeeded.

Stellar-mass black holes (SMBHs), defined as having M_{BH} between 3 and ~ 100 $M_{\odot}$, are believed to be created largely from CCSNe cores, either at the time of explosion or by accreting from a donor star afterwards. The observed population statistics of SMBHs, therefore, should reflect the population statistics of CCSNe. Approximations can be made to match final SMBH mass to initial

[2] The lifetimes of stars massive enough to explode as CCSNe are short enough that on a galactic timescale they can be assumed to die instantly.

progenitor mass; generally studies assume that the entire helium core of the progenitor collapses into the black hole, but the hydrogen envelope is ejected. Helium core mass tracks total star mass, so an analysis of the observed set of SMBHs can be used to back out statistics on the stellar population that formed them. Kochanek (2014) and Clausen *et al.* (2015), apply this strategy, and while they disagree in the details of the probability function, both surveys conclude that a nonzero percentage of CCSNe fail, and that that failure range is likely located in the mass range $\sim 18-27$ $M_\odot$. Sukhbold *et al.* (2015) confirmed that the population statistics of SMBHs require a large percentage of stars to shed their hydrogen envelopes before they die. Some process, or set of processes, must produce at least the $\sim 1 \times 10^{47}$ erg of kinetic energy necessary to eject the envelope, and must occur reasonably often in the failure mass range to reproduce the observed statistics.

1.2.2 Constraints from Theory

The compactness factor (O'Connor and Ott, 2011) is a value computed from the stellar structure immediately surrounding the iron core and meant to estimate the difficulty of explosion. Progenitor stars with more mass concentrated around their iron cores become more difficult to explode because the shockwave expanding outward from the star's center must overcome the ram pressure of material falling inward. The compactness factor is far from monotonic with mass and in fact becomes chaotic in some regimes (Sukhbold and Woosley, 2014), particularly in the range 20 - 28 $M_\odot$. Sukhbold *et al.* (2015) found mass ranges where the explosion failed entirely, located around the ranges 20 - 26 $M_\odot$. Ugliano *et al.* (2012) found that in simplified models using a neutrino lightbulb most failures occurred in the range 18 - 26 $M_\odot$.

Brown and Woosley (2013a) considered the problem from the perspective of nucleosynthesis. As CCSNe are the dominant source of most elements heavier than lithium, the observed abundances of those elements in the universe can be used to place constraints on how many CC-SNe must explode, or at least contribute substantial matter to the interstellar medium. Observations combined with theoretical predictions of the nucleosynthesis from different events allow for the near-complete failure of stars above 25 $M_\odot$ without disrupting overall chemical abundances, and significant failure rates of stars above 18 $M_\odot$ with some adjustments to uncertain parameters.

1.3 Channels for Creating VLE SNe

Taking all this evidence together, it can be reasonably supposed that a) some percentage of CCSNe fail to explode; b) the likelihood of failure is tied to stellar mass and structure; c) the mass range of progenitors most likely to fail is $18-27$ $M_\odot$, with the highest probabilities in the range $22-26$ $M_\odot$. Confirming or contradicting these propositions requires gathering observational data on CCSN failure rates. By definition, in a failure case the standard CCSN explosion mechanism will not produce a major event, but there are many channels by which an evolved massive star can produce a visible transient either just before or during iron core collapse. If the progenitor star was rotating, then a variety of energetic transients might be possible depending on the distribution of angular momentum, ranging from common gamma-ray bursts by the collapsar mechanism (Woosley, 1993; MacFadyen and Woosley, 1999) to long duration x-ray (MacFadyen *et al.*, 2001; Li, 2003) and gamma-ray (Quataert and Shiode, 2012a; Woosley and Heger, 2012) transients.

But what if the star were rotating very slowly or not at all? Various possibilities for envelope ejection have been discussed including pulsations (Woosley and Heger, 2007), acoustic energy transport (Quataert and Shiode, 2012b; Shiode and Quataert, 2014), pulsational-pair instability supernovae (Kasen *et al.*, 2011), violent late burning stages (Woosley and Heger, 2015), and the outbursts of LBVs (Smith *et al.*, 2011). Acoustic energy transport, LBV outbursts, and violent burning stages are the most likely to produce low energy transients; this thesis will discuss an additional mechanism, called here the Nadyozhin-Lovegrove effect, capable of ejecting a hydrogen envelope during a failed CCSN (Lovegrove and Woosley, 2013).

1.4 Outline

Chapter 2 presents theory and simulations of an alternate method of producing a shockwave in an otherwise completely failed CCSN event, showing the shockwave's formation and the resulting transient. Chapter 3 covers the theory of astrophysical shock breakout, its relevance to VLE SNe, and physical considerations particular to the low-energy case. Chapter 4 presents the results of radiation-hydrodynamic shock breakout simulations in VLE SNe and provides template light curves and spectra. Chapter 5 covers existing observational data and future observing prospects for the transients simulated in this work. Chapter 6 summarizes our conclusions and suggests directions for future work.

Chapter 2

Secondary VLE Transients From Neutrino-Mediated Mass Loss in Failed CCSNe

2.1 Theory of Neutrino-Mediated Mass Loss

In this chapter we consider the problem of producing transients in an otherwise failed CCSN. We follow on a suggestion by Nadezhin (1980)[1] which provides a simple mechanism for ejecting at least some mass in supernova progenitors with very weakly bound envelopes, i.e., red supergiants. The mechanism operates as follows: in all but extremely rare super-massive stars, iron core collapse leads to protoneutron star formation (O'Connor and Ott, 2011). Depending on the course of the CCSN, the central object may then either settle down as a neutron star or contract

[1] More commonly romanized as "Nadyozhin."

inside its event horizon and become a black hole. However, after formation, the protoneutron star will attempt to shed its binding energy. This emission takes the form of a neutrino wind and occurs even if the protoneutron star continues to accrete substantial mass while contracting. As frequently noted (Lattimer and Yahil, 1989; Lattimer and Prakash, 2001), this huge energy loss results in a significant decrease in the gravitational mass of the compact object. This mass loss is of order:

$$BE \approx 0.084 \left(\frac{M_G}{\mathrm{M}_\odot}\right)^2 \mathrm{M}_\odot \tag{2.1}$$

where M_G is the gravitational mass of the cold neutron star. This implies a mass loss of approximately 0.2 - 0.5 $\mathrm{M}_\odot$ over a period of several seconds, far shorter than the sound crossing time for the helium and heavy element core. This “mass,” carried by neutrinos, streams out through the presupernova star nearly at the speed of light without interacting appreciably with the outer layers. To the remaining star it appears as if the gravitational potential of the core has abruptly decreased. In response, the star begins to expand. This chapter presents simulations of this mass loss and the resulting expansion to determine whether it is capable of creating a shock with sufficient energy to reach the outer layers of the star and, if it does, to eject mass and form a visible transient. It is important to note that this expansion precedes the loss in support pressure caused by the collapse of the core. That rarefaction passes out through the star on a slower, free-fall time scale, and will not catch up to the shock.

2.2 Simulation Setup

We begin with two presupernova models calculated using the KEPLER stellar evolution code. KEPLER is a Lagrangian 1D implicit hydrodynamics code with the appropriate nuclear physics, mass loss, opacities, and equations of state for studying massive star evolution (Weaver *et al.*, 1978; Woosley *et al.*, 2002). It is not Courant-limited, allowing it to follow a star from its formation to the collapse of its iron core. Because KEPLER uses a Lagrangian grid, it cannot easily implement the absorbing inner boundary condition necessary to accurately follow the infall of the star once a compact object has formed at its center. Once the presupernova models calculated by KEPLER reached supersonic collapse speeds in their cores, they were thus mapped into CASTRO[2] for further study. The CASTRO calculations were done in one dimension with reactions turned off and the central object modeled as a point object with variable mass placed some distance from the simulated volume. An Eulerian grid with constant mesh and spherical geometry was employed. After the collapse had proceeded long enough in CASTRO to allow shock propagation to the base of the hydrogen envelope, the results were then mapped back into KEPLER and the final hydrodynamics and a light curve were calculated.

2.2.1 Central Object Modeling

The hydrodynamics and radiation transport in the region immediately surrounding a protoneutron star or black hole are complex and difficult to model. A realistic simulation of the neutrino transport alone is well beyond the scope of this paper and the outcome would vary with the choice of neutron star equation of state and the dimensionality of the calculation. But our calculations

[2]Code version as of May 2012.

require only the temporal evolution of the central gravitational potential, and thus reasonably good results can be obtained from parametrized calculations using a generic, qualitative description of the neutrino energy loss. The inner boundary of the CASTRO simulation is placed at the outer edge of the pre-collapse iron core, and matter interior to this boundary is treated as a point mass of variable gravity located at the star's center. This point mass starts the simulation equal to the baryonic mass of the initial core matter, i.e., the iron core mass. As time passes that gravitational mass decreases due to neutrino emission and, if no mass were added, would eventually reach the known cold neutron star value for a given baryonic mass and equation of state (Prakash *et al.*, 1997). However, appreciable mass does accrete and leads eventually to formation of a black hole. During the neutron star's accretion phase neutrinos continue to carry away effective mass. Since the simulations neglect rotation, after the black hole forms matter and energy are assumed to flow into it without further emission.

The gravitational binding energy of the maximum stable neutron star mass, the "Tolman-Oppenheimer-Volkoff (TOV) limit" (Oppenheimer and Volkoff, 1939), gives an upper limit to the amount of possible mass loss. Current data place this value around 2.0 to 2.5 $M_\odot$of gravitational mass (Akmal *et al.*, 1998; Demorest *et al.*, 2010). The characteristic time scale for binding energy loss, which is assumed to occur exponentially, is given by the cooling timescale parameter τ_c, taken here to be 3 seconds (e.g. Burrows and Lattimer, 1987). For this simple case, the mass loss rate is

$$\dot{M}_{\mathrm{G}} = \frac{BE}{\tau_c} e^{-t/\tau_c} \tag{2.2}$$

This equation gives an upper bound on the mass loss and therefore on the strength of the transient produced. This model is referred to as the "maximum mass loss" case.

Somewhat more realistically, we can take into account the time till the neutron star reaches the TOV limit and follow the neutrino energy losses that occur during that time only. For each bit of mass that accretes, some fraction of its gravitational binding energy is radiated away promptly, but more is emitted with a delay since the neutrinos must diffuse out. Once the black hole has formed, the neutrino-emitting material falls within the event horizon much faster than the neutrino diffusion timescale, and any energy that has not been released by the time of collapse ends up in the black hole (Prakash *et al.*, 1997; Burrows, 1988).

The protoneutron star is extremely hot and behaves differently than a cold neutron star. We represent the protoneutron star as a low-entropy core surrounded by a hot envelope and track three masses: M_{Gh}, M_B, and M_{th}. M_B is the baryonic mass, i.e. all mass that either was inside the inner boundary at the time of collapse or subsequently accretes through the inner boundary. M_{Gh} is the effective gravitational mass of the hot neutron star, which is *not*, in general, equivalent to M_o, the gravitational mass of a *cold* neutron star with the same baryon content. This is the mass that defines the gravitational potential in the outer part of the star. M_{th} accounts for the extra mass-energy stored in this hot neutron star as opposed to a cold one due to its higher internal energy and inflated radius. This extra internal energy diffuses away on the cooling timescale τ_c. The gravitational mass M_{Gh} of the hot neutron star is then:

$$M_{Gh} = M_o + M_{th} \tag{2.3}$$

$$= M_B - BE_c + M_{th} \tag{2.4}$$

where BE_c is the cold neutron star binding energy. As matter accretes a fraction ϵ of the subsequent change in binding energy is assumed to be trapped and added to M_{th} while the remaining fraction 1

- ϵ is radiated promptly as neutrinos. The trapped energy then diffuses out on the cooling timescale τ_c. The evolution of M_{th} is thus given by

$$\dot{M}_{th} = -\frac{M_{th}}{\tau_c} + \epsilon \frac{d\,BE_c}{dM_B}\,\dot{M}_B \tag{2.5}$$

and the initial condition $M_{th} = BE_c$. The derivative $d\,BE_c/dM_B$ is evaluated from the binding energy equation, Eq. 2.1. Once all M_{th} has diffused away, i.e. the neutron star has cooled, Eq. 2.4 reduces to the standard cold neutron star equation $M_G = M_B - BE_c$. Assuming rapid virialization of the accreted material implies that the parameter ϵ should not exceed ~ 0.5. As the cooling timescale at the surface is likely less than the timescale for the full protoneutron star, ϵ is likely to be much lower. In the limit that the cooling timescale were much shorter than the accretion timescale, ϵ would go effectively to zero. For our models we adopt $\epsilon = 0.1$. In Section 2.3.3 we test the effects of varying this parameter and find them to be small.

Neutrino emission halts when the neutron star has accreted past the TOV maximum mass limit. However this limiting mass must be adjusted for the neutron star's evolving heat content. Therefore we wait until the cold core of the neutron star ($M_{Gh} - M_{th}$) has accreted past the TOV limit before we assume the core has become a black hole and shut off the neutrino emission. From this point on the central object behaves as a purely gravitational point mass that absorbs all of $\dot{M}_B$. This is referred to as the "full loss" model, as it is the most physically accurate of our models.[3]

Figure 2.1 shows an example of the full model implemented in RSG15 with TOV = 2.5 $M_\odot$. The blue curve shows M_B, the total baryonic mass that has entered the core region (precollapse core plus accretion); it is higher than the black curve showing M_{Gh}, the effective gravitational mass

[3] This is not to say that the full loss model includes all physical processes involved; far from it. But this analytic model captures the gross behavior of the central object over time, and that is the relevant quantity in this work.

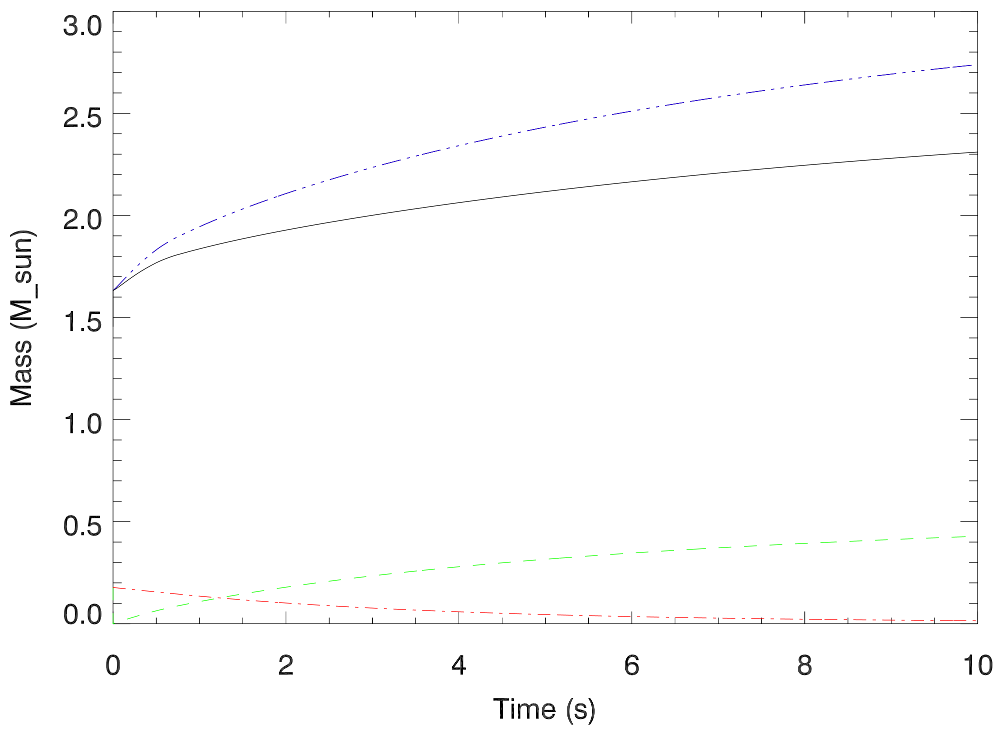

Figure 2.1: Core mass growth in the 15 $M_{\odot}$ model RSG15 with an assumed TOV mass limit of 2.5 $M_{\odot}$, demonstrating the "full loss" model. The black curve (solid) shows M_{Gh}, the gravitational mass. Blue (dash-triple dot) is M_B, the baryonic mass. Red (dash-dot) is the thermal mass M_{th}. Green (dashed) shows the cumulative lost mass from the simulation.

Table 2.1: Stellar Model Parameters

Model	Final Mass ($M_\odot$)	He Core Mass ($M_\odot$)	He Core Radius (cm)	Compactness $\xi_{2.5}$
RSG15	12.79	4.27	3.568×10^{10}	0.18
RSG25	15.84	8.20	1.807×10^{10}	0.33

of the core. The red curve shows M_{th}, which decays exponentially as the protoneutron star cools. The green curve shows the cumulative mass loss in the simulation. Even though the core in this case persists for nearly 24 s before collapsing to a black hole, most of the mass loss occurs during the first 5 seconds.

2.2.2 Choice and Structure of Stellar Models

The two presupernova models used for this paper were red supergiants with a ZAMS mass of 15 $M_\odot$ (RSG15), shown in Fig. 2.2, and 25 $M_\odot$ (RSG25), shown in Fig. 2.3, both of solar metallicity. They are taken from the survey of Woosley and Heger (2007). Both stars lose substantial mass before reaching the end of their lives. Based on the observational and theoretical constraints discussed in § 1.2, we expect a 25 $M_\odot$ star to be more likely to fail than a 15 $M_\odot$ star. But the 15 $M_\odot$ star represents a much more common supernova progenitor, and thus even if this mass has a low failure probability it may still produce a significant number of events. The 25 $M_\odot$ model has a more compact structure and may be more likely to make a black hole promptly. Model RSG15 has a helium core of 4.27 $M_\odot$ that extends to 3.568×10^{10} cm. RSG25 has a helium core of 8.20 $M_\odot$ that extends to 1.807×10^{10} cm. Both red supergiants have a large, tenuously-bound hydrogen envelope extending from the helium core out to $\sim 5 \times 10^{13}$ cm. The net binding energy of the envelope external to what is nominally the helium core (where the hydrogen mass fraction

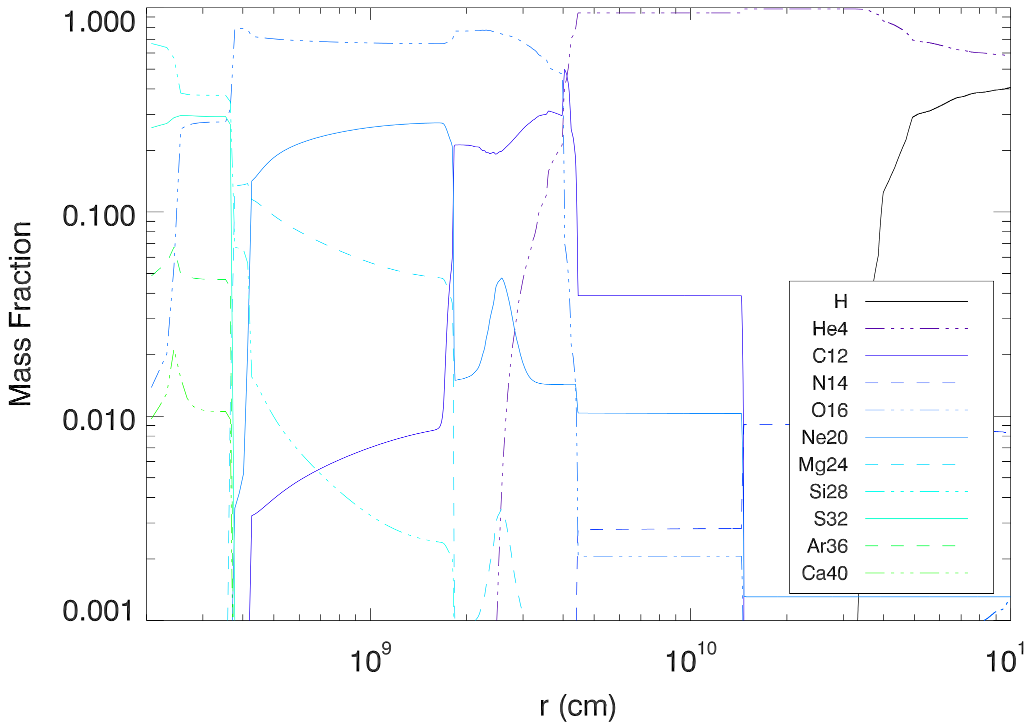

Figure 2.2: Composition of the RSG15 supernova progenitor star.

declines to 1%) is 1.1×10^{48} erg, but a short distance out at 4.48 $M_\odot$ this declines to 10^{47} erg, a value that characterizes most of the hydrogen envelope. These values include internal energy but not the energy potentially available from recombination. For the 25 $M_\odot$ model, the net binding energy external to the helium core is 6.4×10^{48} erg, but this declines to 10^{47} erg when the interior mass increases from 8.20 $M_\odot$ to 8.36 $M_\odot$and a still smaller value characterizes most of the envelope. We note that the recombination of 10 $M_\odot$ of hydrogen (13.6 eV per atom) would release 2.6×10^{47} erg.

Some additional parameters of both models can be found in Table 4.2. Also given is the compactness parameter, $\xi_{2.5}$, as defined by O'Connor and Ott (2011), but computed at the time when the star is moved to CASTRO rather than at the time of core bounce. A star with a higher compactness parameter has a denser region surrounding its core; for our purposes, this means it will accrete to the TOV limit faster and therefore potentially lose less mass as neutrinos.

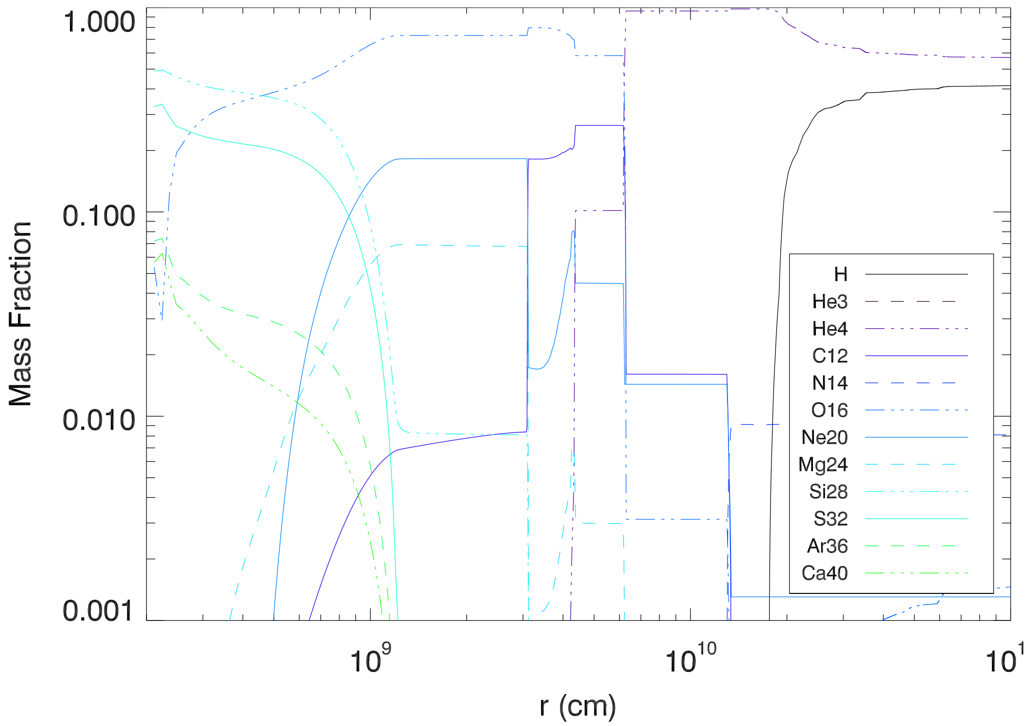

Figure 2.3: Composition of the RSG25 supernova progenitor star.

Because of the extended size of the red supergiant progenitors, we do not carry the entire star on our simulation grid in CASTRO. Instead we model only the helium core and base of the hydrogen envelope.

2.3 Hydrodynamic Response

2.3.1 Models Without Neutrino Mass Loss

Without an outgoing shock or mass loss from neutrinos, the inner layers of the star should collapse directly into the black hole. This scenario provides an excellent check of the fidelity of our simulation. As Figure 2.4 shows, our model accurately reproduces this behavior. Dark (purple) colors on the plot indicate early times, shading to light (red) colors at late times. Initially the bulk of

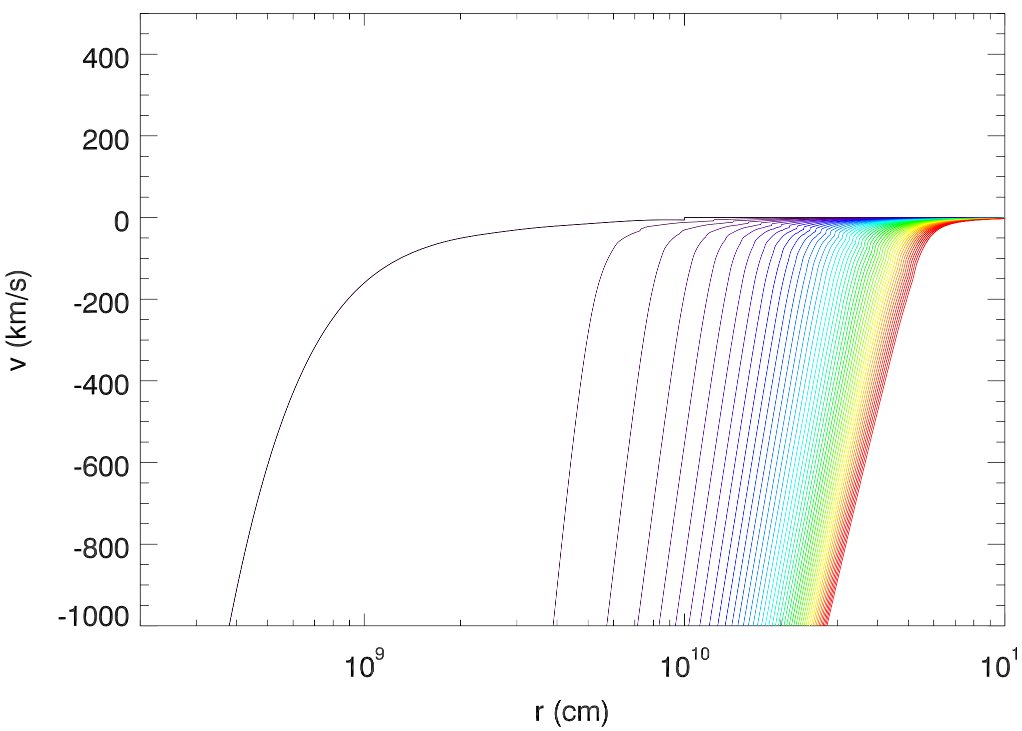

Figure 2.4: Velocity curves showing collapse of the RSG15 stellar model in the prompt black hole formation case, i.e. without any mass loss. Positive velocities are outwards, negative are inwards. Curves are purple (light) for early times, shading to red (dark) for late, approximately 15 s spacing. With no mass decrement and no core bounce shock to provide outward velocity, the star simply falls into the black hole. Total time shown: 709 s.

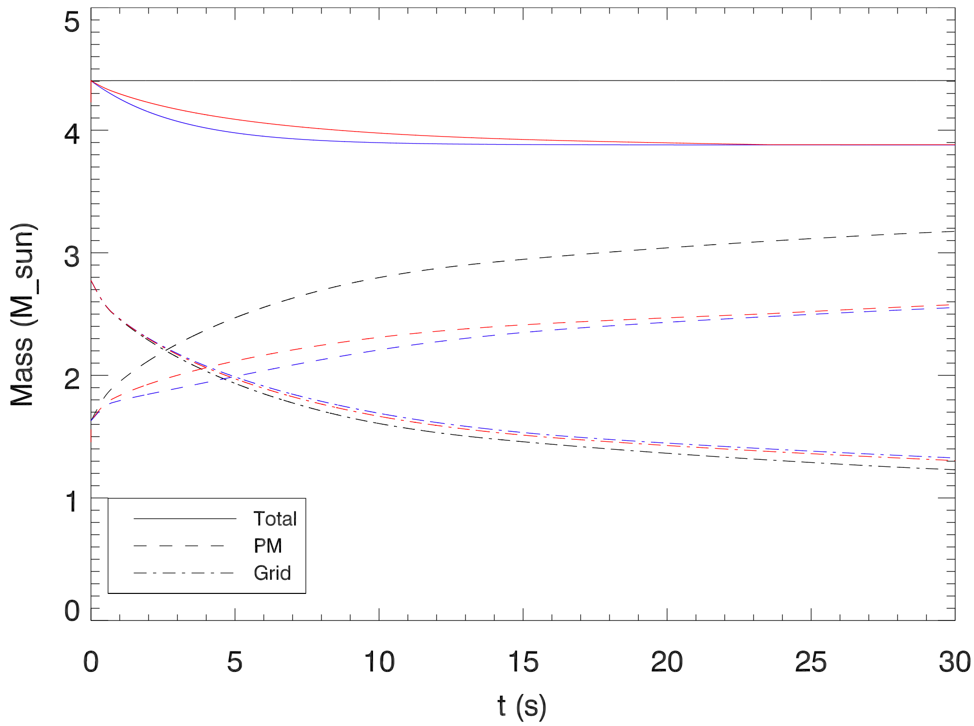

Figure 2.5: Various core masses as a function of time for Model RSG15 and a TOV limit of 2.5 $M_\odot$. The central mass M_{Gh} (dashed) grows while the mass on the simulation grid (dot-dashed) drops. The solid line represents the total mass in the center and on the grid combined. Black curves show the no neutrino loss (constant mass) case. Blue curves show the maximum-loss model, while the red curves show the full neutrino loss model.

the star is in hydrostatic equilibrium (zero velocity) with a small portion near the core showing high infall velocities. As the collapse continues, more and more of the stellar material acquires negative velocities. Without an outgoing shock to counter this motion, it eventually falls into the core. If the simulation is run for long enough, all mass will disappear from the grid. Physically this scenario corresponds to prompt black hole formation, when the core collapses without passing through an intermediate protoneutron star stage. If the outer layers of the star do not have sufficient angular momentum to form a disk when they reach the black hole, the entire star will disappear without producing a transient - the unnova case as defined by Kochanek *et al.* (2008).

Figure 2.5 shows the growth of the simulated point mass in RSG15. The black curves show the model with no neutrino mass loss; in this case the point mass corresponds to M_B. The dashed line represents the growth of the point mass while the dot-dashed line shows the mass on the simulated grid (remember that the point mass itself is outside the grid). Over time this point mass grows as the grid mass declines, with most of the change occurring in the first 15 seconds. The solid line shows the sum of the point mass and grid mass, i.e. the total mass represented in the simulation; in the no-mass-loss case it is constant throughout. This confirms that our simulation is reproducing the collapse accurately without spurious shocks or unphysical mass loss.

2.3.2 Models With Maximum Neutrino Mass Loss

The set of blue curves in Figure 2.5 shows the mass evolution using the simplified maximum mass loss model. In this case, the point mass corresponds to M_G with losses defined by Eq. 2.2, in which the core loses the total binding energy appropriate to a TOV-limit neutron star on a time scale τ_c, regardless of the amount of mass falling in from the collapsing star. This model therefore provides an upper bound on possible transients, as the core cannot lose more mass than the binding energy of the largest possible neutron star. The amount of mass lost in each case is listed in Table 2.2. Following the blue curves in Figure 2.5, as the collapse begins the point mass growth (dashed) is noticeably suppressed for the first 5 seconds as neutrino losses balance accreted mass. The overall mass in the simulation (solid) drops accordingly, then becomes constant as mass loss ceases.

This mass decrement was sufficient to produce an outgoing shock in the inner layers of the 15 $M_\odot$ presupernova star. The shock's evolution is shown in Figure 2.6 (purple at early times, shading to red at late times). The shock grows in speed as it leaves the helium core and succeeds in reaching the base of the hydrogen envelope. Of interest is the fact that the shock strength varied

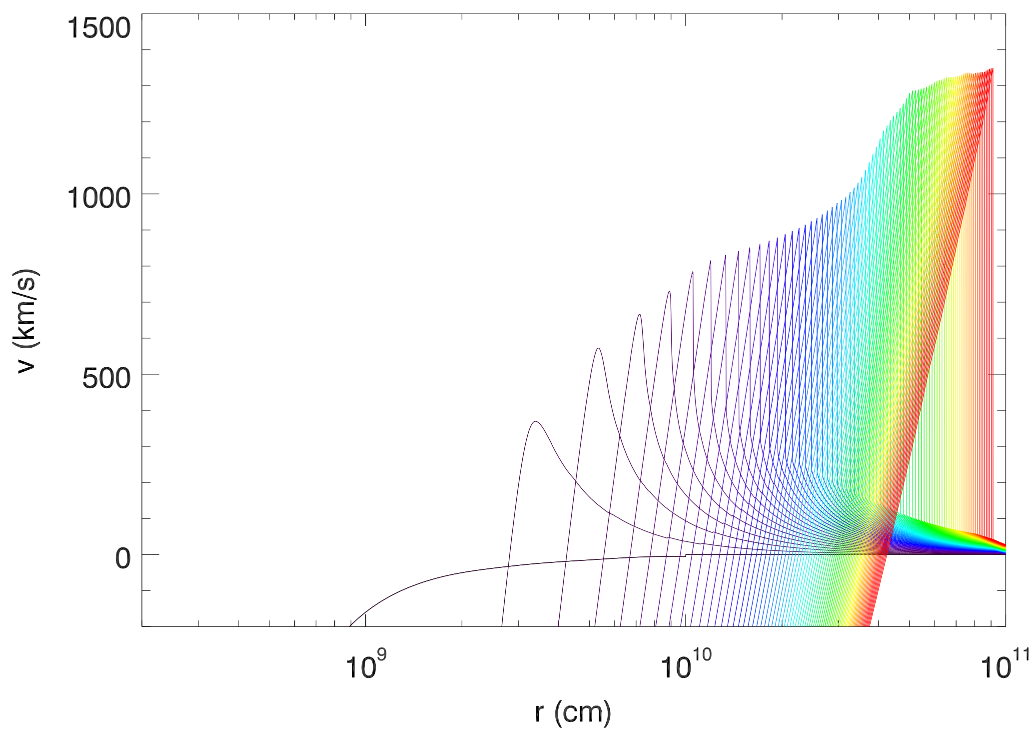

Figure 2.6: Collapse of the RSG15 model in the maximum neutrino mass loss case, showing a shock forming due to the effective core mass decrement. Positive velocities are outwards, negative are inwards. Curves are purple for early times, shading to red for late. This model has the TOV limit set to 2.5, resulting in a mass decrement of 0.525 $M_\odot$. The shock propagates out of the helium core ($r = 3.568 \times 10^{10}$ cm). Time shock reaches 10^{10} cm: 38 s. Time to end of helium core: 196 s. Time to 10^{11} cm: 577 s.

Table 2.2: Maximum Mass Loss Models

Stellar Model	TOV ($M_\odot$)	Mass Lost ($M_\odot$)	KE[a](ergs)	Shock Strength[b](km/s)
RSG15	2.0	0.336	1.875×10^{47}	902
...	2.1	0.370	2.599×10^{47}	985
...	2.2	0.407	3.572×10^{47}	1070
...	2.3	0.444	4.855×10^{47}	1158
...	2.4	0.484	6.554×10^{47}	1249
...	2.5	0.525	8.719×10^{47}	1341
RSG25	2.0	0.336	6.537×10^{46}	723
...	2.1	0.370	1.002×10^{47}	820
...	2.2	0.407	1.483×10^{47}	919
...	2.3	0.444	2.139×10^{47}	1025
...	2.4	0.484	3.011×10^{47}	1134
...	2.5	0.525	4.148×10^{47}	1246

[a] At base of hydrogen envelope

[b] At $r = 10^{11}$ cm

noticeably with the choice of neutron star upper mass limit. The approximate shock strengths at 10^{11} cm for our six different choices of TOV limit are listed in Table 2.2.

2.3.3 Models With Realistic Neutrino Mass Loss

The red curves in Figure 2.5 show the mass evolution for the full model for neutrino losses described in Section 2.1. In this case the dashed line showing the point mass corresponds to M_{Gh} as given by Eq. 2.4. This model takes into account the thermal mass loss and links the cessation of neutrino losses to the amount of material accreted by the core rather than switching it off after a predetermined timescale, as in the upper bound model. As can be seen in Figure 2.5, this model (red) loses mass over a longer timescale than the maximum loss model (blue), continuing until the point mass reaches the TOV limit, in this case 2.5 $M_\odot$, after which the total mass becomes constant. We expect equal or less mass loss in this case as compared to the maximum loss model. In the

Table 2.3: Full Mass Loss Models

Stellar Model	TOV ($M_\odot$)	Mass Lost ($M_\odot$)	KE[a](ergs)	Shock Strength[b](km/s)
RSG15	2.0	0.277	1.287×10^{47}	814
...	2.1	0.331	2.059×10^{47}	926
...	2.2	0.382	2.953×10^{47}	1019
...	2.3	0.430	3.911×10^{47}	1094
...	2.4	0.477	4.896×10^{47}	1157
...	2.5	0.523	5.779×10^{47}	1204
RSG25	2.0	0.179	8.418×10^{45}	394
...	2.1	0.230	2.893×10^{46}	569
...	2.2	0.281	6.581×10^{46}	725
...	2.3	0.331	1.204×10^{47}	866
...	2.4	0.382	1.930×10^{47}	996
...	2.5	0.433	2.827×10^{47}	1114

[a] At base of hydrogen envelope

[b] At $r = 10^{11}$ cm

case where the TOV limit is high enough that the neutron star lives for longer than the cooling timescale, the core loses close to the maximum possible amount of mass; in the case where it does not, however, mass loss is suppressed as neutrinos that would have been emitted instead end up inside the black hole. The amount of mass lost in each case is listed in Table 2.3.

Though the overall mass decrement in the full model cases is lower than in the maximum loss case, it is still sufficient to produce an outgoing shock. Figure 2.7 shows the shock evolution for RSG15, TOV = 2.5 $M_\odot$. The approximate shock strengths at 10^{11} cm for our six different choices of TOV limit are listed in Table 2.3. The six shocks created in RSG15 are shown in Figure 2.8.

We also tested variations in the parameter ϵ controlling the fraction of binding energy trapped as thermal mass. Changes in ϵ have a small but real effect on the total mass loss, depending on the amount of accreted mass. The more mass accreted, the more important ϵ will be. As higher TOV limit models tend to accrete longer, ϵ has a higher impact here. A lower ϵ leads to a higher

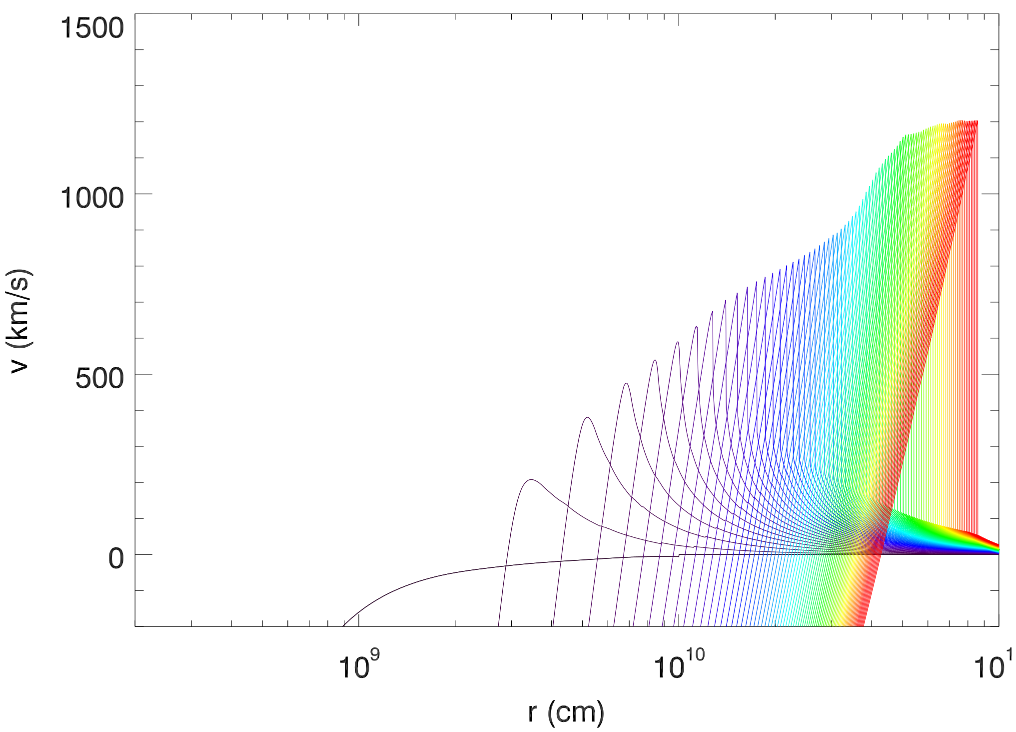

Figure 2.7: Collapse of the RSG15 model in the fully-modeled neutrino mass loss case, showing a shock forming due to the effective core mass decrement. Positive velocities are outwards, negative are inwards. Curves are purple for early times, shading to red for late. This model has the TOV limit set to 2.5, resulting in a mass decrement of 0.523 $M_\odot$. The shock is smaller in strength than the maximum-loss case and reaches the edge of the simulation with a lower velocity. Time shock reaches 10^{10} cm: 40 s. Time to end of helium core: 207 s. Time to 10^{11} cm: 620 s.

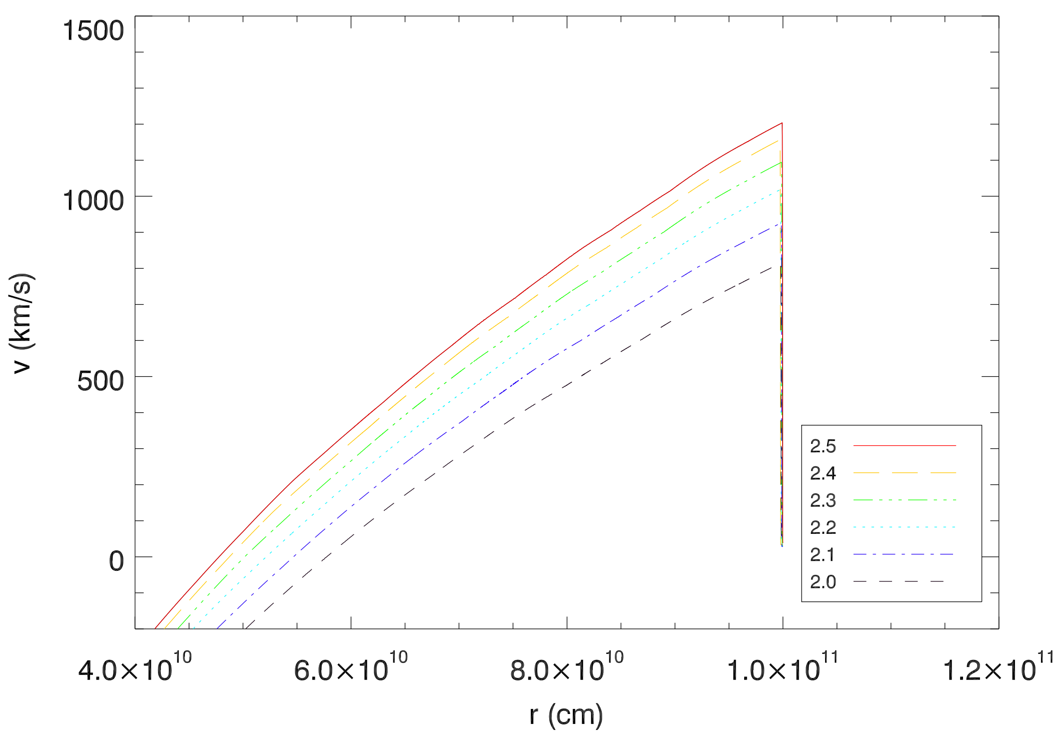

Figure 2.8: RSG15 shocks at the limit of the CASTRO simulated domain for six different choices of TOV limit, full neutrino loss model. The upper curve corresponds to TOV = 2.5 $M_\odot$, the lowest to TOV = 2.0 $M_\odot$. Other curves are spaced by 0.1 $M_\odot$.

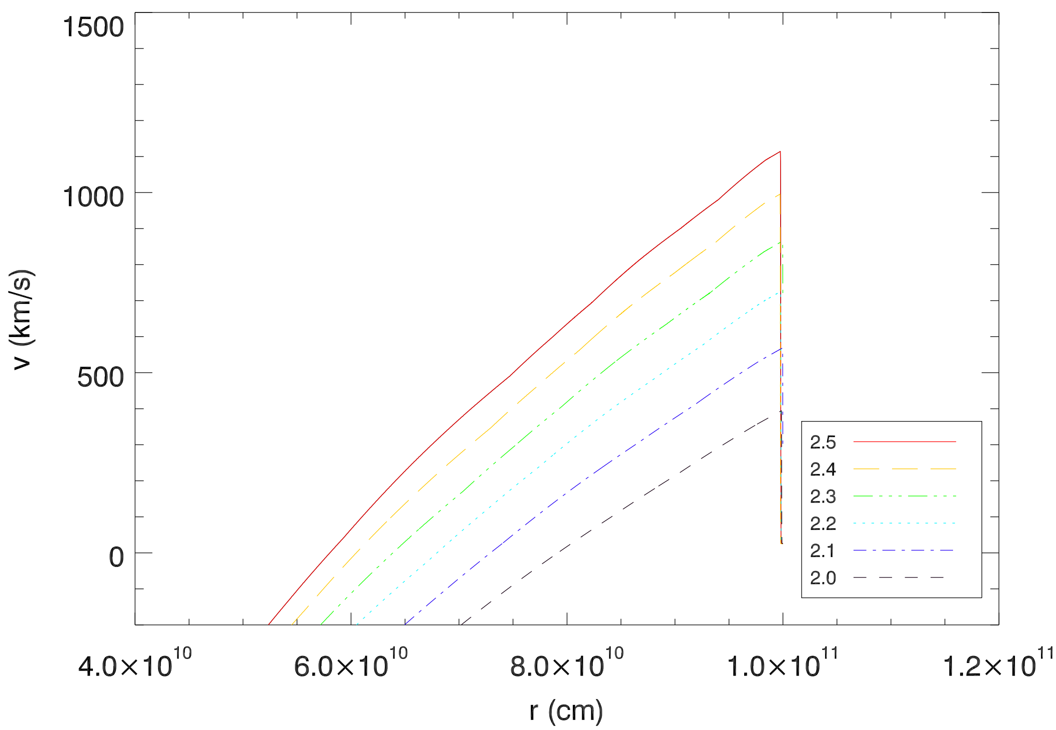

Figure 2.9: RSG25 shocks at the limit of the CASTRO simulated domain for six different choices of TOV limit, full neutrino model. The choice of TOV limit has a stronger effect on the final shock strength in this model than it does in RSG15. The upper curve corresponds to TOV = 2.5 $M_\odot$, the lowest to TOV = 2.0 $M_\odot$. Other curves are spaced by 0.1 $M_\odot$.

mass loss as less of the binding energy is temporarily trapped as thermal mass. We tested the range $\epsilon < 0.5$, identified as the physically reasonable range of this parameter. For the case where the TOV limit is 2.5 $M_{\odot}$, the most sensitive, a change of 0.05 in ϵ in RSG25 resulted in approximately a 0.011 $M_{\odot}$ change in the overall mass loss. In the extreme case $\epsilon = 0.5$, this will make a TOV = 2.5 $M_{\odot}$ model look like a TOV $\sim$ 2.35 $M_{\odot}$ model. For lower TOV limits, the effect of varying ϵ was smaller. Thus, although a change in ϵ will affect the mass decrement and by extension the shock strength, the overall results are robust.

2.3.4 Effects of Stellar Structure

The kinetic energy of the shock that reaches the hydrogen envelope is strongly influenced by the size of the presupernova core and the overlying stellar structure through which it must travel. This is best illustrated in simulations using the maximum mass loss model, since the mass decrement is the same regardless of stellar structure. Even though both stars experience the same gravitational change, the final shock in RSG25 models is significantly weaker than in RSG15 since it must traverse a much heavier carbon-oxygen and helium core before reaching the hydrogen envelope.

Additional effects come into play when using the full neutrino model that terminates emission based on the core's accretion. RSG25 has a denser inner structure (higher compactness) and a more massive iron core of 1.83 $M_{\odot}$, compared to 1.63 $M_{\odot}$. As it therefore accretes faster than RSG15 and is already closer to the TOV limit, the core of RSG25 spends significantly less time in the protoneutron star state; consequently the same choice of parameters in the larger star causes less mass loss. The full mass loss model in RSG25 also shows systematically lower mass decrements than the maximum mass loss model in all cases, indicating that even in cases with a high TOV limit and a relatively long-lived protoneutron star not all the binding energy is being emitted before

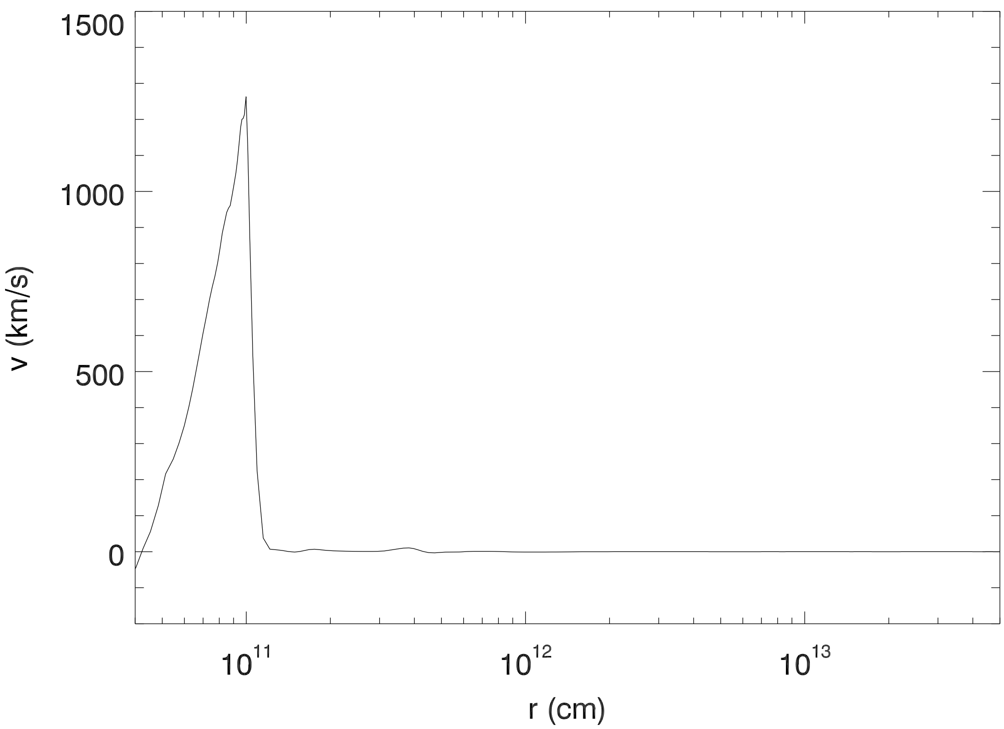

Figure 2.10: Shock modeled by CASTRO in RSG15 (TOV = 2.5, full neutrino losses) mapped into KEPLER.

collapse to a black hole. The six shocks produced in RSG25 are shown in Figure 2.9.

2.4 Transients Produced

In the case of prompt black hole formation in a star without a high-J outer layer, the core collapse itself produces no shock and no visible transient - the star simply disappears. However, we have shown that in cases where a protoneutron star forms, an outgoing shock can be created regardless. Can this shock produce a detectable transient, intermediate between a complete disappearance and a traditional explosion, as raised by Kochanek *et al.* (2008)? To evaluate this question we took models from CASTRO where the shock had reached 1×10^{11} cm (the limit of the simulation) and mapped them back into KEPLER, then continued to evolve them. Figures 2.10 and 2.11 show the

KEPLER results for RSG15, TOV = 2.5; Figure 2.10 shows the shock mapped in from CASTRO, and Figure 2.11 shows the final velocity of the hydrogen envelope at $t = 5 \times 10^7$ s.

The shock has decreased significantly in strength by the time it reaches the base of the hydrogen envelope, but this envelope is very tenuously bound in both RSG15 and RSG25. For each model we tested six choices of TOV limit (2.0 - 2.5 $M_\odot$, in 0.1 $M_\odot$ increments) and evaluated the strength of the shock that reached the hydrogen envelope. Using the full neutrino loss model, we found that in every case tested for RSG15 and in 3 of 6 tested for RSG25 that the shock produced was larger than 1×10^{47} ergs, the approximate binding energy of the envelope (see Table 2.3). We can therefore realistically expect the envelope to be ejected in these cases. However, the highest kinetic energy achieved was only of the order of 6×10^{47} ergs, and most models fell well below that number. The envelope is therefore ejected with a very low velocity (50 - 100 km/s). It emits most of its energy via hydrogen recombination. Optically this transient has a low luminosity $\sim 10^{39} - 10^{40}$ ergs/s, but maintains this luminosity for of order a year. The color temperature of the transient is very red, of order 3000 K. An example light curve can be seen in Figure 2.12 for RSG15, TOV = 2.5.

The transients calculated here are obviously much fainter and less energetic than standard core-collapse supernova, but they do bear some similarity to a class of recently-observed transients: the “luminous red novae," such as V838 Mon (Munari *et al.*, 2002). Luminous red novae are too bright to be ordinary classical novae, but too faint and red to be supernovae. A survey such as that proposed by Kochanek *et al.* (2008), monitoring red supergiants for anomalous transients that might signal the birth of a black hole, should catch these events. They would be visible as a sudden brightening of the “star" for of order a year, followed by a gradual but complete disappearance. This

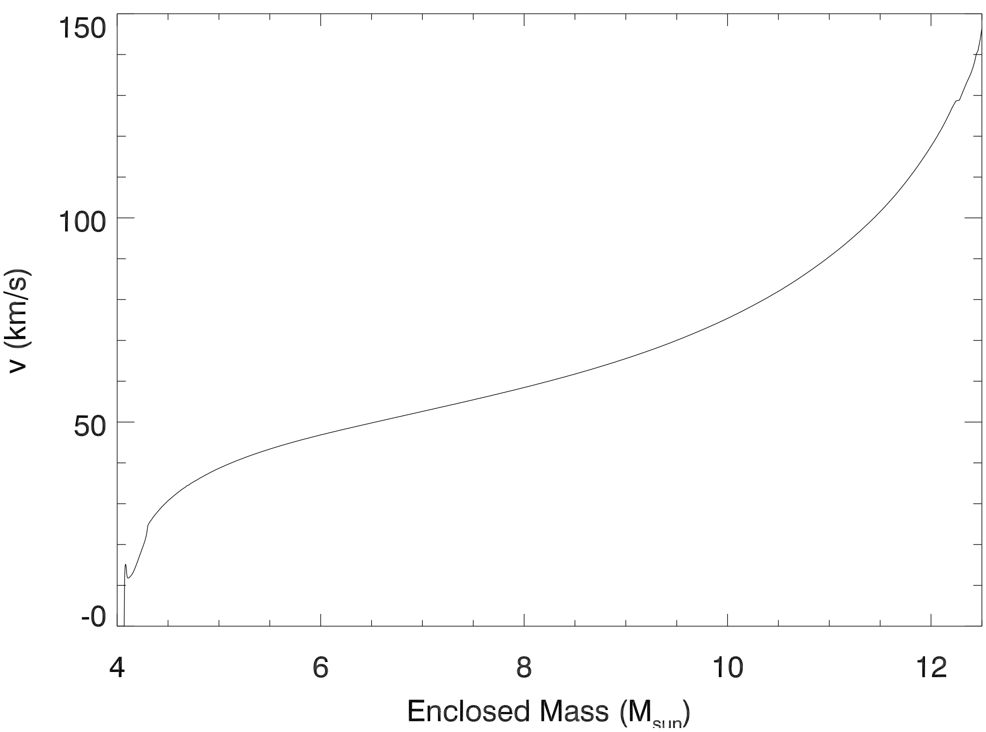

Figure 2.11: Velocity of the hydrogen envelope at 5×10^7 s after core collapse in RSG15, TOV = 2.5, full neutrino loss model, evolved further in KEPLER.

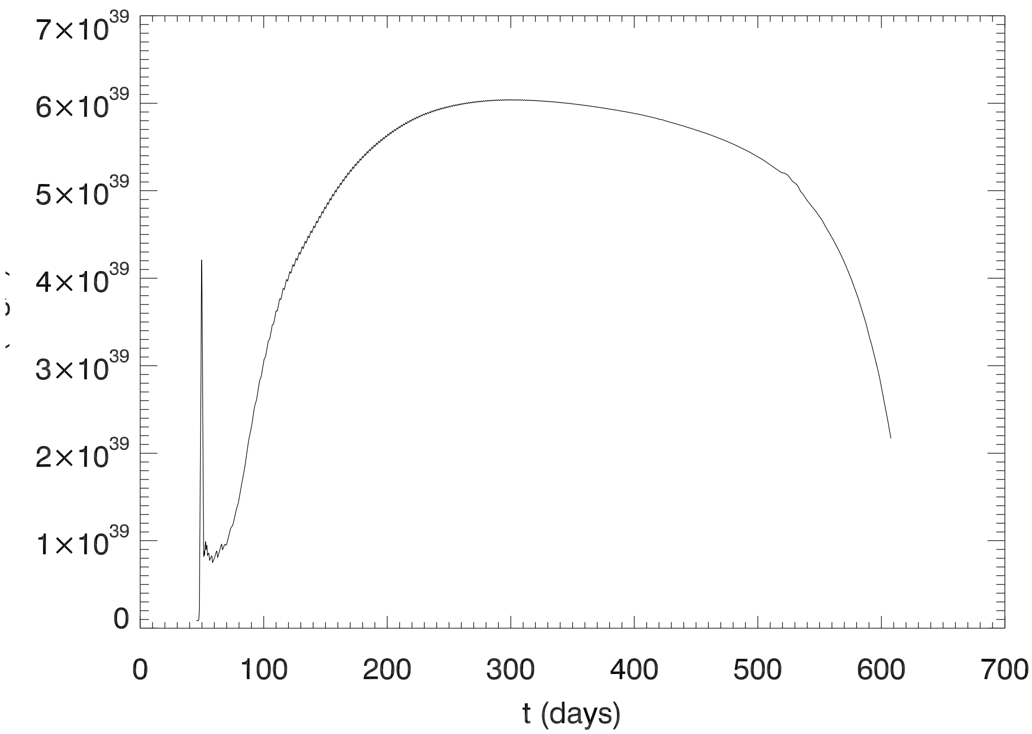

Figure 2.12: KEPLER light curve for a transient from RSG15, TOV = 2.5. The transient is low luminosity but lasts for around a year.

scenario will be discussed further in Chapter 6.

In RSG25 a TOV limit of 2.2 $M_{\odot}$ or lower resulted in such weak outgoing shocks that they could not be accurately followed using KEPLER, and would probably be unable to eject the envelope. In situations where the envelope is not ejected, there is still the possibility of a transient at late times if the envelope is rotating. As it falls back into the black hole, the massive envelope may create a disk and potentially a long-duration gamma-ray transient as described by Woosley and Heger (2012). Since the most massive stars are the ones more likely to produce black holes quickly, it remains possible to produce these long gamma-ray transients. This type of transient, while invisible in the optical, could emit low levels of gamma rays for months.

A higher TOV limit in the neutron star EOS increases the probability of these transients occurring. Holding the TOV limit constant, the final strength of the shock is highest in stars with both smaller initial iron core masses (more time spent as a neutron star) and smaller carbon-oxygen and helium core masses. We might therefore expect the strongest transients to come from the lowest-mass red supergiants that fail to form CCSNe. Nucleosynthetic constraints place a lower limit on the maximum mass star that must explode as a supernova most of the time. Brown and Woosley (2013b) sets this limit at between 20 and 25 $M_{\odot}$. Stars above 20 $M_{\odot}$ become more difficult to explode, as measured by their compactness parameter (O'Connor and Ott, 2011), and hence more likely to fail. At the same time, in stars above 25 $M_{\odot}$, it will become increasingly difficult for the shock to reach the surface. We may therefore expect the progenitors of these transients, if they do occur, to land in the range 20 - 25 $M_{\odot}$.

For heavier stars that lose their hydrogen envelope and die as WR stars, or for stripped progenitors in binaries, a shock can form and may reach the surface, depending on the size of the remaining helium core. Without a large envelope to eject, the transient will be brief but brighter.

2.5 Conclusions

We have demonstrated that iron core collapse in a massive star is capable of producing a faint observable transient even if the collapse itself creates no prompt outgoing shock. The mass lost to neutrinos results, in some cases, in a shock sufficient to unbind the hydrogen envelope. For a given parametrization of the neutrino losses, the transient produced becomes weaker as the TOV mass limit is reduced and as the mass of the presupernova helium core increases. It therefore remains possible, depending upon the TOV limit assumed, to fail to eject the envelope in more massive stars. If the star in these cases has sufficient angular momentum in its outer layers, it may instead produce long gamma-ray transients as described by Woosley and Heger (2012); otherwise it will disappear as an unnova as described by Kochanek *et al.* (2008). The amount and history of the neutrino mass loss has a strong effect on the magnitude of the shock produced, as does the structure of the carbon-oxygen and helium cores of the progenitor star. In the two red supergiant models tested, the shock reached the base of the hydrogen envelope in a majority of the models with enough energy to eject it. These unusual transients will appear as low-energy, long-duration, red events as the ejected envelope emits its energy via hydrogen recombination. The ejected envelope has a speed on the order of 50 - 100 km/s and maintains a luminosity $10^{39} - 10^{40}$ ergs/s for approximately a year.

Chapter 3

Shock Breakout Transients and Considerations for Low-Energy Events

3.1 Shock Breakout as a Detection Mechanism

VLE SNe, no matter how they are caused, are by definition faint and hence challenging to observe. The shock breakout transients accompanying these events are much better candidates for detection. Astrophysical shock breakout occurs when the leading edge of a shockwave erupts through a star's surface. As the outgoing shock propagates through the star, radiation builds up behind its optically thick leading edge. When the surrounding matter reaches a sufficiently small optical depth, this radiation is released on a relatively short timescale to produce a bright flash. This flash is the second indication, after the neutrino pulse, that a core-collapse supernova has occurred. Because their properties are determined by the star's structure in a thin layer near the surface, shock breakouts carry unique information about the progenitor's surface gravity, radius, and composition that is wiped out by the subsequent explosion (or collapse).

Other quantities, like mass, radius, and opacity, being equal, Popov (1993) and Kasen and Woosley (2009) predict that the luminosity of a Type IIp supernova during its plateau stage scales as $E_{\rm exp}^{5/6}$. Thus a supernova with explosion energy $E_{\rm exp} \sim 10^{48}$ erg would have a luminosity 300 times fainter than a typical Type IIp supernova with $E_{\rm exp} \sim 10^{51}$ erg, or about 10^{40} erg s^{-1}. The duration of the plateau, which goes as $E_{\rm exp}^{-1/6}$, would be 4.6 times longer, or about 400 days. Shock breakout transients are as a rule shorter and brighter than the supernovae that follow. The breakout from a 10^{48} erg explosion would have a typical luminosity of 10^{42} erg erg s^{-1} and last about half a day. Unlike breakout in common supernovae, the temperature in a VLE SN is low and a larger fraction of the energy would be emitted longward of the Lyman limit, and the transient will last significantly longer. These qualities make them better candidates for detection. Observing the shock breakouts of VLE SNe can give occurrence rates for this sort of supernova as well as constrain the properties of the presupernova star and the explosion energy.

In the case of shock breakout, the radiation spectrum is expected to be a dilute blackbody, i.e. it has a blackbody form but peaks at a different wavelength than would be predicted from the radiation energy density. In this paper the temperature computed from a simple $E_r = aT^4$ relation is called the "effective temperature" T_e, while the Wien's law temperature corresponding to the emitted spectrum's peak wavelength is the "color temperature" or "spectral temperature" T_c. The ratio T_c / T_e is set by stellar structure and opacity and is, as will be seen, a parameter of great interest.

Simulating shock breakout is not a simple task. The simulation code must model hydrodynamic shockwaves, track radiation-material interactions, and be capable of stably transporting radiation in both optically-thick and optically-thin regimes. There are also particular challenges specific to the low-energy regime which will be discussed in detail later in this chapter. The largest theoretical question mark in these simulations is the treatment of opacity, which fundamentally governs the shape and behavior of the breakout flash. This chapter details the physical processes modeled in our VLE SNe shock breakout survey; the results of this survey are given in Chapter 4.

3.2 Previous Studies

3.2.1 Regimes Considered

Shock breakout has been considered analytically by several papers, including (but by no means limited to) Klein and Chevalier (1978), Nakar and Sari (2010), Rabinak and Waxman (2011), Matzner and McKee (1999), and Katz *et al.* (2010), and it is worth investigating what work has been done on the general theory of shock breakout as well as on the specific case of VLE SNe. Klein and Chevalier (1978) and Katz *et al.* (2010) both focus on X-ray emission in standard-energy breakouts in compact progenitors, so while the general physics are still applicable, the numerical results are not. Rabinak and Waxman (2011) does not explicitly study breakout, focusing instead on the UV & optical lightcurve during the supernova's initial expansion phase, but the densities and temperatures in this regime are comparable to those in VLE SNe and they give numerical results useful to the models considered here. Nakar and Sari (2010) performs analytic calculations that are then applied to standard-energy CCSNe in a variety of progenitors, as well as shock waves breaking out of white dwarves; again, while the results may not be applicable, the general theory is still relevant. Piro (2013) is the only paper to consider the specific case of VLE SNe, following on discussions of the transients modeled in Lovegrove and Woosley (2013). The equations provided in Piro (2013) for predicting shock breakout luminosity and observed temperature are tested here in § 4.5.2.

Shock breakout has previously been simulated in models for SN1987A (Ensman and Burrows, 1992; Tolstov *et al.*, 2013), Type Ib and Ic SNe (Tolstov *et al.*, 2013), Type IIp supernovae (Tominaga *et al.*, 2011), and pair instability supernovae at cosmic distances (Kasen *et al.*, 2011; Whalen *et al.*, 2013). Ensman and Burrows (1992) (hereafter EB92) modeled breakout in SN1987A using the VISPHOT code, a 2T Lagrangian code. Tolstov *et al.* (2013) (hereafter T12) performed calculations for a similar SN1987A progenitor, as well as calculations for breakout in Type Ib/Type Ic SNe, using the STELLA code; STELLA is a Lagrangian code with multigroup radiation transport. STELLA was also used by Tominaga *et al.* (2011), in this case to model breakout in red supergiants at standard Type IIp energies. Kasen *et al.* (2011) simulated explosions using the KEPLER Lagrangian code and calculated lightcurves using SEDONA, which implements Monte Carlo techniques for radiation transport; while Whalen *et al.* (2013) used the RAGE code from Los Alamos National Laboratory (LANL), a 2T Eulerian code with multigroup capabilities. Breakout as a general phenomenon has therefore been robustly simulated by many different codes implementing different radiation transport schemes, having in common the ability to handle separate gas and radiation temperatures, and, in cases where color temperature is calculated directly, multigroup or other multifrequency transport. However, again, the bulk of the explosion models used in all these works have energies ≥ 1.0 B.

3.2.2 Opacity Calculations

The studies mentioned in the previous section use a wide variety of methods to calculate opacities. Whalen *et al.* (2013) used the OPLIB database from LANL and SEDONA has a mixture of analytic and tabulated opacities; unfortunately, the events considered are in significantly different regimes of energy and metallicity than VLE SNe, and their opacity calculations are likely not useful.

STELLA, used in Tolstov *et al.* (2013) and Tominaga *et al.* (2011), has opacity routines that handle free-free, bound-free, and line opacities, and the results in the Type IIp case have some relevance to the RSG models studied here.

Some of the authors mentioned in the previous section assumed electron scattering as the dominant opacity source: EB92 used tables to calculate a total opacity, then calculated electron scattering and subtracted that value from the tabulated opacity to get absorptive opacity, and Rabinak and Waxman (2011) used a similar procedure with different tables. Nakar and Sari (2010) assume a Kramer's Law form for the absorptive opacity.

3.2.3 Color Temperature

There are two methods for deriving T_c: direct calculation of the spectrum, which requires a multifrequency code; or making the assumption that T_c is set to the gas temperature at some radius, then calculating that radius, which can be done in 2T codes. EB92, which used a 2T code, used the latter method and recovered temperature ratios T_c/T_e on the order of 2 - 3 for simulations of SN1987A. Klein and Chevalier (1978) ran 1D non-local-thermodynamic-equilibrium simulations without coupled hydrodynamics and recovered a ratio around 3. Both T12 and Tominaga *et al.* (2011) used STELLA's multigroup transport to directly calculate spectra and reported ratios in the same 2 - 3 range. Analytically, Nakar and Sari (2010) predict color temperature (which they call "observed temperature") ratios on the order of 1.8 (RSG) to 2.1 (BSG).[1] Rabinak and Waxman (2011) perform numerical calculations in service of their predictions and predict a T_c/T_e ratio in the range 1.1 - 1.8.

[1] Nakar and Sari (2010) disagree strongly with the use of T_e, which they maintain is not an observable quantity and of no physical interest. Nevertheless, they do calculate these ratios, and it is included in our results as well.

A small sample of candidate shock breakout observations have been published in the literature. Most are X-ray detections of events in compact progenitors. A few are in RSGs, and the Kepler satellite recently published two possible optical breakout candidates. These events are clearly not VLE SNe and are less relevant to the physics under consideration, and their detailed discussion is postponed until § 5.4.

3.3 CASTRO-Radiation

Because realistically modeling shock breakout requires advanced radiation transport, it is useful to discuss the specific capabilities of CASTRO-Radiation and how they apply to this problem. CASTRO uses a flux-limited diffusion (FLD) transport scheme for radiation. The diffusion approximation for radiation closes the transport equations by assuming a Fick's Law diffusion relation between radiation energy density E_r and flux $\vec{F}$, $\vec{F} = \vec{\nabla} E_r$. This approximation renders the equations tractable but breaks down outside of optically-thick regions. When the material becomes optically thin, the diffusion treatment leads to superluminal velocities and produces unphysical behavior. To avoid this, the equations can be modified to incorporate a flux limiter, λ, that forces the correct limiting behavior in both the diffusive and free-streaming regimes and allows a stable transition between them (Levermore and Pomraning, 1981a). Propagation velocities will not exceed the speed of light and the pressure tensor will have the correct limiting behavior. This approximation allows a stable modeling of the crucial transition between optically-thick and optically-thin material that shapes the breakout flash.

Grey or two-temperature ("2T") radiation transport models radiation as a fluid with a temperature T_r. T_r can vary from the gas temperature, but the radiation spectrum is assumed to be thermalized at all times (i.e. a blackbody with temperature T_r). The multigroup approximation (MGFLD) divides the frequency range of interest into a number of energy bins and calculates transport separately for each, with coupling terms to allow energy to move between bins. Thus multigroup transport, unlike 2T transport, allows the radiation to have any spectrum so long as it is resolvable by the number of simulated groups. In the case of shock breakout this allows T_c and T_e to differ, which in turn allows the direct study of the ratio between these two quantities. For further details on MGFLD and its specific implementation in CASTRO, see Krumholz *et al.* (2007) (derivation) and Zhang *et al.* (2011) (implementation).

3.4 Spectral Effects Due to Velocity

Most theoretical work on the subject assumes that so long as the radiation remains coupled to the gas, the radiation temperature also reflects the gas temperature (see Nakar and Sari (2010), Appendix B, for the reasoning behind this). However, initial shock breakout simulations for this work produced unexpectedly high radiation temperatures, particularly a spike at the shock front where gas temperature remained steady but T_c increased by an order of magnitude. This can be explained through a consideration of the different terms affecting the spectrum in the FLD approximation.

3.4.1 Analysis

During breakout, two terms in the radiation-hydro equations dominate the spectrum: an advection term in frequency space and the matter-radiation coupling term. The multi-group treatment of flux-limited diffusion takes the form:

$$\frac{\partial E_g}{\partial t}+\vec{\nabla}\cdot\left(\frac{3-f_g}{2}E_g\vec{v}\right)-\vec{v}\cdot\vec{\nabla}\left(\frac{1-f_g}{2}E_g\right)= \tag{3.1}$$

$$c\kappa_g(\alpha T^4-E_g)+\vec{\nabla}\cdot\left(\frac{c\lambda}{\chi_R}\vec{\nabla}E_g\right) \tag{3.2}$$

$$+\int_g\frac{\partial}{\partial\nu}\left[\left(\frac{1-f}{2}\vec{\nabla}\cdot\vec{v}+\frac{3f-1}{2}\hat{n}\hat{n}:\vec{\nabla}\vec{v}\right)\nu E_\nu\right] \tag{3.3}$$

$$-\frac{3f-1}{2}E_g\hat{n}\hat{n}:\vec{\nabla}\vec{v} \tag{3.4}$$

Consider first the optically thick limit where the gas has the most influence on the radiation, in which case $f_g = 1/3$ and all $\hat{n}\hat{n}$ terms (representing freestreaming radiation) disappear.

$$\frac{\partial E_g}{\partial t}+\frac{4}{3}\vec{\nabla}\cdot E_g\vec{v}-\frac{1}{3}\vec{v}\cdot\vec{\nabla}\left(E_g\right)= \tag{3.5}$$

$$c\kappa_g(\alpha T^4-E_g)+\vec{\nabla}\cdot\left(\frac{c}{3\chi_R}\vec{\nabla}E_g\right) \tag{3.6}$$

$$+\frac{1}{3}\int_g\frac{\partial}{\partial\nu}\left[\left(\vec{\nabla}\cdot\vec{v}\right)\nu E_\nu\right] \tag{3.7}$$

On the left-hand side, the first term in the equation represents the quantity to be solved for, the change in group energy with time. The second and third terms represent energy transfer by bulk fluid motion. The three terms on the right-hand side respectively represent energy exchange via absorption/emission, diffusion of radiation, and energy transfer between frequency groups.

This equation can be interpreted as an advection equation in frequency space (see Zhang *et al.* (2013) for details). The "sound speed" in this medium includes a term dependent on the divergence of velocity, $\nabla\cdot\vec{v}$. In practice, this means that as the gas is compressed by the shock, velocity divergence shifts the spectrum towards the blue. This term can cause the radiation spectral temperature to diverge from the gas temperature even in optically thick regions. In particular, the spectrum will harden significantly just before breakout as the shock reaches the stellar atmosphere and increases in velocity. The magnitude of this effect is directly linked to the velocity at the shock front - higher velocity leads to greater divergence and more hardening of the spectrum. Conversely, the absorption-emission source exchange term, which depends on absorptive opacity, will tend to equilibrate the radiation and the matter, so in the case of shock breakout it will cool the radiation. The relative strength of these two terms determines the ultimate color temperature. If the source exchange term dominates, T_c will follow the gas temperature. If the advection term dominates, however, T_c can be significantly higher. Therefore the relative timescales of these terms must be considered in order to ensure the resulting color temperature has the correct qualitative behavior.

Let the scale length $L = c/\chi_R \vec{v}$ where χ_R is the total opacity (which in these simulations is $\approx$ scattering opacity). The terms that will alter the spectrum are the frequency group coupling term $(1/3)(\vec{\nabla} \cdot \vec{v})\nu E_g$, which depends on velocity divergence, and the absorption/emission energy exchange term $c\kappa_P(\alpha T^4 - E_r)$. The time scale of the exchange term is the inverse of $c\kappa_P$. The time scale of the velocity divergence term is the inverse of $\vec{v}/3L$.

$$\tau_x^{-1} = c\kappa_P$$

$$\tau_v^{-1} = \frac{v}{3L} = \frac{1}{3} v \left(\frac{\chi_R v}{c} \right)$$

$$\frac{\tau_v}{\tau_x} = \theta = (c\kappa_P) \left(\frac{3c}{\chi_R v^2} \right) = 3 \left(\frac{c}{v} \right)^2 \left(\frac{\kappa_P}{\chi_R} \right)$$

If $\theta > 1$, $\tau_v > \tau_x$, the exchange term dominates, and the radiation spectral temperature will follow the gas. If $\theta < 1$, $\tau_v < \tau_x$, the velocity term dominates, and the radiation spectral temperature will increase above the gas temperature in regions of high velocity divergence, e.g. shock fronts.

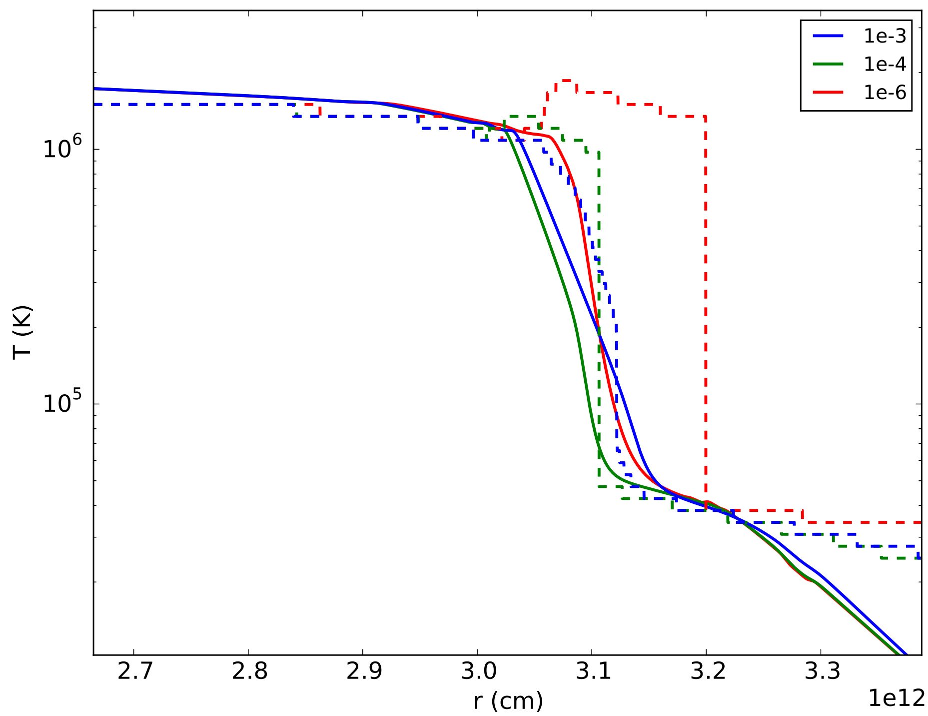

Figure 3.1: Temperatures in SN1987A shock breakout for the 1.0 B model with three choices of $\epsilon = 1 \times 10^{-6},\ 1 \times 10^{-4},\ 1 \times 10^{-3}$ (red, green, blue). Solid lines show gas temperature and dashed lines show radiation spectral temperature as estimated by measuring which frequency group has the highest energy density. At low ϵ (red, green), the high velocity divergence at the shock front causes the spectral temperature to increase above the gas temperature even when the material is still optically thick. As ϵ increases, radiation-gas energy exchange counteracts the effects of the velocity divergence and the spectral temperature stays in equilibrium with the gas temperature longer. At high ϵ (blue), the exchange term dominates and the spectral temperature follows the gas temperature through the hydrodynamic shock. The stair-step nature of the color temperature curves is an artifact of the multigroup approximation, where radiation is represented by a set of groups each corresponding to a range of frequencies. A color temperature calculation done by selecting the group with the highest energy density and applying Wien's Law to its central frequency will therefore show discrete changes in value corresponding to the boundaries of the frequency groups.These calculations are shown very close to the moment of breakout, when radiation has just begun to diffuse out from behind the shock.

3.4.2 In Simulation

For a model of SN1987A at breakout, $v \sim 15000$ km s^{-1}. If $\kappa_P/\chi_R = 10^{-6}$, $\theta = 0.0012$; if κ_P/χ_R increases to 10^{-3}, then $\theta = 1.2$, implying a significant shift in the spectral behavior of the simulation. Figure 3.1 shows the temperatures of three SN1987A simulations run up to the moment of breakout in order to test this hypothesis. Solid lines represent gas temperature and dashed lines represent color temperature. Where the two lines overlap, the radiation and gas are in equilibrium. The red and green dashed lines, representing color temperature in simulations with $\epsilon = 10^{-6}$ and 10^{-4} respectively, both spike above the gas temperature at the shock front, the region of highest velocity divergence. By contrast in the $\epsilon = 10^{-3}$ simulation (blue) the color temperature follows the gas temperature through the hydrodynamic shock. The stair-step appearance of the T_c curves is an artifact of the multigroup approximation; these simulations used 64 frequency groups spaced logarithmically in the range 1×10^{15} - 1×10^{18} Hz.

Shock front velocities in the red supergiant models, especially the VLE explosions considered here, are much slower than in SN 1987A. Velocities at breakout range from 80 to 1200 km s^{-1} for RSG15. and 150 to 500 km s^{-1} for RSG25. Even for $\kappa_P/\chi_R = 10^{-6}$ the exchange term dominates in most RSG cases. Velocity effects are therefore unlikely to play a role in VLE SNe breakouts. However, in cases with high velocity, low metallicity, or both, this effect may come into play.

3.5 Opacity Processes

Shock breakout is fundamentally shaped by the optical thick-thin transition layer in the star's atmosphere and modeling it requires great attention be paid to the simulated opacities. Unfortunately, detailed opacity calculations are neither simple nor straightforward. Existing studies, as noted in § 3.2, have often used tabulated opacities or assumed the dominance of electron scattering. This is an accurate assumption at standard supernova energies where temperatures behind the shock will be in the range 1×10^5 - 1×10^7 K, but it begins to break down in the regime explored by low energy events. For VLE SNe breakouts, we expect temperatures in the range 1×10^4 - 5×10^5 K and densities in the range 1×10^{-9} - 1×10^{-12} g/cm^3. At these conditions different opacity processes begin to play a role, and the tabulated opacities used by many supernova and stellar evolution codes do not extend to the low-density regime, requiring the code to do its own opacity calculations. This section discusses major opacity processes, their effects on both regular and low-energy shock breakout, and their treatment in these models.

In all following discussions of opacity we assume both electrons and ions to be at the single gas temperature T tracked by CASTRO. CASTRO does not track electrons and ions separately.

3.5.1 Free-Free Processes (Compton scattering and bremsstrahlung)

Analytic Representation

At the temperatures, densities, and metallicities explored in this paper, the predominant contribution to scattering opacity comes from photons colliding with free electrons (Compton scattering), which in these low-energy models can be considered solely in the Thomson limit. This process also contributes to absorption opacity because these collisions are not perfectly elastic and a small amount of energy is exchanged between photon and electron. The energy exchanged per

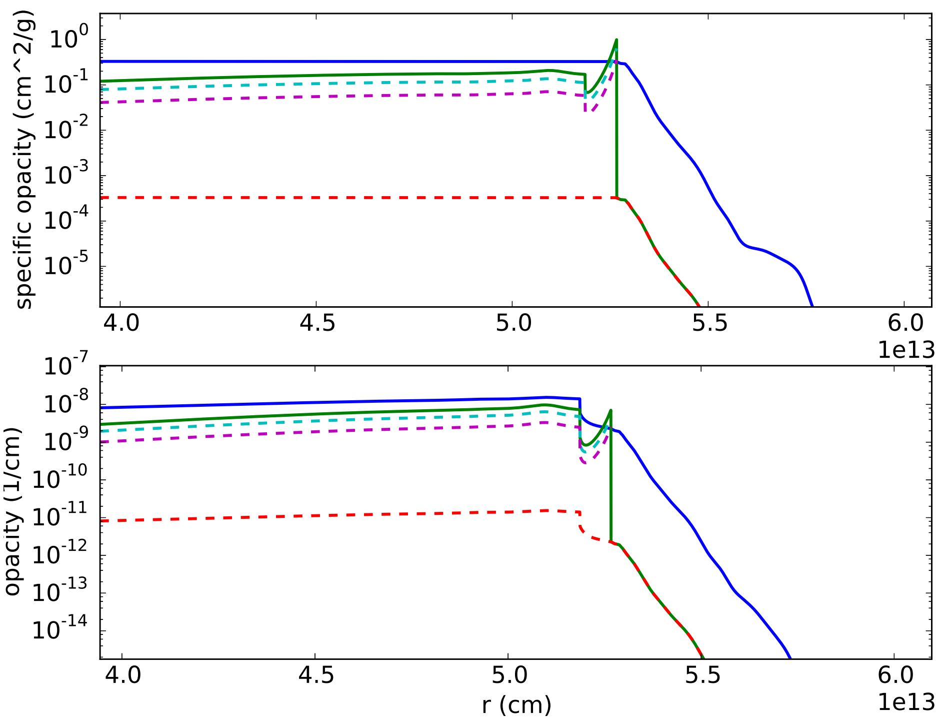

Figure 3.2: Opacity profiles for model B15 near breakout, showing specific opacity κ (top) and opacity $\kappa\rho$ (bottom). Solid lines show total opacity (blue) and total absorptive opacity (green). Dotted lines show absorptive opacity contributions from Compton scattering (red), inverse bremsstrahlung (cyan), and bound-free (magenta).

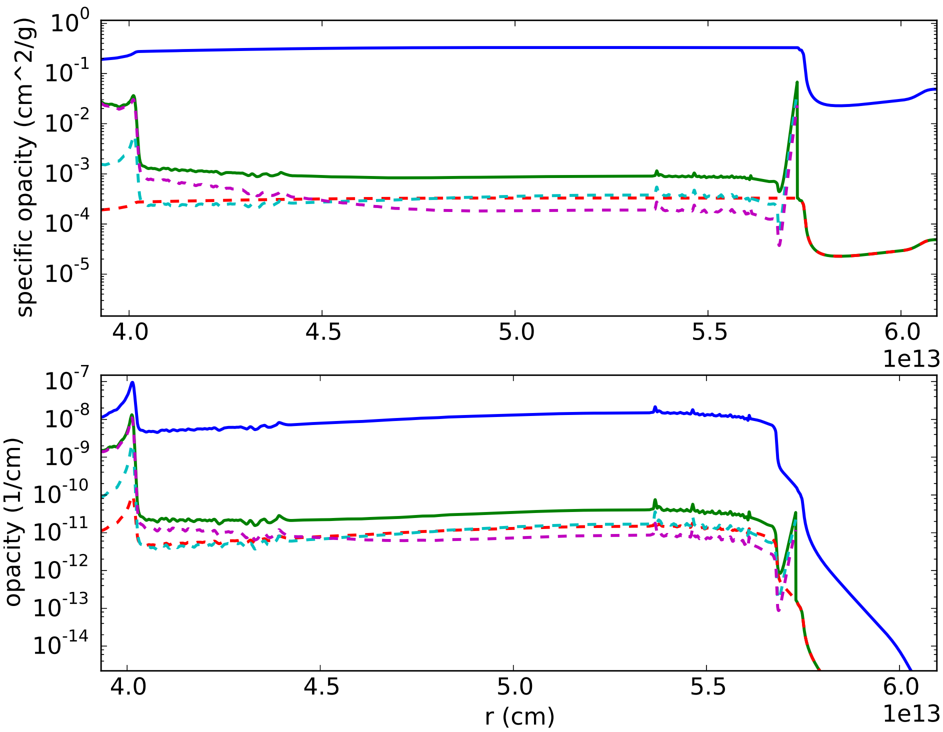

Figure 3.3: Opacity profiles for model F15 near breakout, showing specific opacity κ (top) and opacity $\kappa\rho$ (bottom). Solid lines show total opacity (blue) and total absorptive opacity (green). Dotted lines show absorptive opacity contributions from Compton scattering (red), inverse bremsstrahlung (cyan), and bound-free (magenta).

collision is:

$$\Delta E = \frac{h\nu}{m_e c^2}(4kT_g - h\nu) \tag{3.8}$$

where T_r is the radiation temperature. If the photon energy $h\nu$ is less than the gas/electron energy $4kT_g$ then the photons will gain energy (the inverse Compton process); otherwise they will lose energy to the gas. As the radiation temperature drops, the average photon energy $h\nu$ does as well, and each scattering exchanges less energy. If the only absorption source considered is Compton scattering, then as the breakout energy drops absorption will become inefficient at equilibrating the radiation. The simulation will therefore show the chromosphere retreating within the star to higher temperatures and densities, increasing the T_c/T_e ratio. This will be discussed further in Chapter 4.

Bremsstrahlung emission occurs when an electron passes close to another charged particle, generally an atomic nucleus, and the change in its energy causes the emission of a photon. There is an associated inverse bremsstrahlung process wherein a photon strikes an electron moving near a nucleus and causes an increase in its energy. This results in a transfer of energy from radiation to gas and therefore functions as an absorptive opacity. Inverse bremsstrahlung in regions with fully ionized hydrogen and helium follows a Kramer's Law opacity and can be calculated analytically as:

$$\kappa_{P\,b} = C_b T^{-3.5} n_e n_i l^2 \tag{3.9}$$

where C_b is a numerical constant and l is the ionization level of the nucleus.

While Compton scattering depends only on the electron number density n_e, since it considers only photons scattering off electrons, inverse bremsstrahlung depends on both n_e and n_i as both an electron and an ion are involved in each interaction. For a completely ionized atmosphere consisting of mostly hydrogen and helium, $n_i \approx n_e$. This gives $\kappa_{P\,b} \propto n_i^2$, and in fully ionized regions $\rho \approx n_i \mu$ where μ is the mean molecular weight, resulting in a ρ^2 dependency. Inverse bremsstrahlung therefore drops off more rapidly with ρ than Compton scattering, relevant since shock breakout takes place in a region of sharply decreasing density. The steepness of this density profile is a property of the progenitor star and therefore does not differ between standard CCSNe and VLE SNe.

The gas temperature at the shock front, however, does vary significantly between standard CCSNe and VLE SNe. Compton scattering depends linearly on gas temperature, but inverse bremsstrahlung goes as $\propto T^{-3.5}$. Thus a small drop in temperature causes inverse bremsstrahlung opacity to increase much faster than Compton scattering, fast enough to overcome the suppression from the ρ^2 term, making inverse bremsstrahlung much more significant in models at lower temperatures. In the VLE case temperatures during breakout are on the order of 5×10^4 - 3×10^5 K, and in this regime inverse bremsstrahlung plays a significant role and must be considered in simulation.

Implementation

Energy exchange via photon-electron collisions occurs at the same rate as electron scattering. The CASTRO opacity network used for breakout represents absorptive opacity from Compton scattering as a fraction of electron scattering opacity $\kappa_C = \epsilon\chi_e$, where χ_e is the Thomson electron scattering opacity and ϵ is some factor < 1.0. In our simulations ϵ is generally in the range 1×10^{-3} - 1×10^{-4}.

For inverse bremsstrahlung calculations the CASTRO opacity network implements eq. (3.9). Note that this approximation becomes invalid if hydrogen and helium are not fully ionized. When the gas temperature drops below approximately 4.5×10^4 K, helium and hydrogen begin to recombine, and this equation gives progressively more unreasonable answers as inverse bremsstrahlung no longer follows a Kramer's Law form. The opacity network therefore stops calculating bremsstrahlung opacity below this temperature.

3.5.2 Bound-Free Processes (photoionization)

Photoionization is a complex process. Because cross-sections for ionization depend strongly on the energy of the incoming photon, precise formulas for this opacity are heavily frequency-dependent. However, above 5000 K hydrogen may be assumed to be ionized, and above 4.5×10^4 K helium may also be assumed to be completely ionized. Therefore when $T > 4.5\times10^4$ K only metals will contribute to photoionization opacity. In a star of solar metallicity the fraction of the atmosphere that consists of metals is small, but their large cross-sections and low ionization energies make their opacities significant. In this regime the photoionization can be treated as a grey opacity with a Kramer's Law form.

$$\kappa_{P\,p} = 4.34\times10^{25}\,Z(1.0+X_H)\rho T^{-3.5} \qquad (3.10)$$

where X_H is the hydrogen mass fraction and Z the metal mass fraction (not the proton number). However, this raises the question of how to treat photoionization when $T < 4.5\times10^4$ K. Here the Kramer's Law opacity breaks down and truly accurate calculations are quite time-intensive. An approximate grey opacity may be found by doing a number of frequency-dependent calculations and taking their Planck mean, but this is again quite time-intensive. It is therefore worth considering whether photoionization opacities below the helium ionization limit are relevant; in these models the opacity network ceases to calculate bound-free opacities below this temperature.

3.5.3 Bound-Bound Processes (line opacities)

Line opacities are not accounted for in these simulations. Based on extrapolation from existing models, the fraction of opacity contributed by bound-bound is expected to be of order 10% of the other absorptive opacities. This is likely not significant enough to change overall behavior, but would be of interest to add. However, this requires either generating tables for the appropriate temperature and densities regimes, which, as noted, is challenging, or manually implementing a much larger opacity network that would be by necessity frequency-dependent, obviating the work done to place other opacities in simpler grey forms and requiring lengthy multigroup simulations for even the bolometric light curves. Thus bound-bound opacities are not implemented in these models.

3.6 Opacity and Color Temperature in VLE Models

Color temperature is not directly set by some requirement of shock breakout physics. As discussed in § 3.2, many (but not all) numerical simulations of breakout predict a ratio of 2-3 between T_c and T_e. Nakar and Sari (2010) predict a ratio 1.8 in red supergiants and 2.1 in blue supergiants and in Rabinak and Waxman (2011), which considers a low-temperature phase of the supernova akin to conditions during a VLE SN breakout, ratios are calculated to be in the range 1.1 - 1.8. It is reasonable, therefore, to ask what kind of ratio can be expected in the VLE case.

In the following analysis it is important to distinguish between the optical depth as measured from the stellar surface, denoted as τ', as opposed to the optical depth of a single shell, denoted simply τ. In a simulation context a "shell" is assumed to refer to one cell of a 1D spherical model, each cell having a single value for both opacity and density. τ is therefore equal to $\kappa\rho\Delta r$.

The criterion used in Nakar and Sari (2010) to determine if a shell of gas will set the radiation's color temperature to its local gas temperature is whether said shell can produce sufficient photons to create a blackbody spectrum before the radiation diffuses through it. Nakar and Sari (2010) use this criterion to create the parameter η, which is the ratio of the number of photons a shell must produce in order to set the radiation to its local gas temperature, divided by the number of photons that can be produced in the appropriate time:

$$\eta = \frac{n_{BB}}{t_s \dot{n}_\gamma} \tag{3.11}$$

where t_s is the time radiation spends in the shell, which is at minimum $\Delta r/c$. While the photons are propagating in the diffusive regime, the time they spend in each shell is $\tau\Delta r/c$. If $\eta < 1$, the shell can produce sufficient photons and it will thermalize the radiation. The emitted peak color temperature therefore reflects the gas temperature of the outermost shell still coupled to the radiation and having $\eta < 1$, which is here called the chromosphere R_c. In the limit that radiation spends a full diffusion time in each cell, Nakar and Sari (2010) notes that the condition $\eta = 1$ is equivalent to each photon experiencing at least one absorption in the shell, placing the chromosphere at the location where $\tau_a \tau \approx 1$.

Shock breakout begins when $\tau' \approx c/v_s$ and the radiation can escape the star ahead of the shock. Opacity drops steeply in the post-shock region and once radiation can travel ahead of the shock it will escape from the rest of the star without further interaction. Thus the condition $\tau' = c/v_s$ is also the condition $\tau = c/v_s$ and the corresponding shell is the photosphere of breakout.[2] If $\tau \approx \tau_a$, then $\eta = 1$ is $\tau_a^2 \approx 1$ and R_c should now be at $\tau_a \approx 1$. However, the breakout criterion is

[2] Assuming that the medium around the star is transparent to the breakout flash. This is assumed to be true in the models considered here, but in the case of stars with dense CSM/strong stellar winds, it may not be, and the photosphere may be external to the star entirely. The modeling of breakout in stars with complex CSMs is of great interest, but well beyond the scope of this work.

now $\tau_a \approx c/v_s$. As $c/v_s > 1$, this would place R_p at a higher optical depth, i.e. a smaller radius, than R_c; but R_c cannot exceed R_p since past R_p the radiation no longer spends a diffusion time in each cell and on average is not expected to interact. Thus as long as $\tau_a \approx \tau$, $R_c \approx R_p$ and $T_c \approx T_e$.

A typical shock velocity near the surface in a compact progenitor and a standard-energy model is 1.5×10^4 km/s. At this velocity breakout would occur at $\tau = c/v_s = 20$ and $R_c \leq R_p$ as long as $\tau_a/\tau \leq 0.05$. Typical values for this ratio in these cases are 0.01 and lower. Note that since the temperature is changing rapidly in the post-shock region, R_c does not have to be much smaller than R_p to give $T_c > T_e$. In the low energy models the shock velocity is lower and the absorptive opacity is higher due to the low-T effects on opacity as discussed in § 3.5. At $v = 5 \times 10^3$ km/s breakout would occur at $\tau = 100.0$ and $R_c \leq R_p$ only if $\tau_a/\tau \leq 0.01$, and a typical ratio of such optical depths near the surface is closer to 0.5.

In SN1987A, the highest ratio between absorptive depth and total depth is about 0.01. In G15, it is 0.04. But in E15 (10^{50} erg) it is 0.5, and in B15 (10^{48} erg) it is as high as 0.7. Thus the color temperature can be expected to converge with the effective temperature as the shock temperatures go down. This results in a breakout even brighter in the IR and optical windows than would be expected. The observational impacts of this effect are discussed in § 5.1.

3.7 Effects of Metallicity

What effect does metallicity have on the ratio T_c/T_e at breakout? While a full simulated exploration of this space is beyond the scope of this paper, we can qualitatively predict some behavior. Stars with high envelope metallicities and/or low shock velocities will likely show the 2 - 3 ratio, but stars with very low envelope metallicities, such as Pop III stars, might exhibit spectral temperatures dramatically higher than predicted due to the velocity divergence effects discussed in § 3.4. Kasen *et al.* (2011) estimated the shock velocity at breakout in a pair-production SN in a red supergiant model at 1.5×10^4 km/s, similar to the SN1987A model discussed in § 3.4.2; in blue supergiants this number can be substantially higher. At the temperatures of a standard-energy breakout inverse bremsstrahlung is highly suppressed and metals contribute most of the photoionization opacity; total absorption opacity in a metal-poor star may therefore be quite low. At high velocities and low absorptive opacity the velocity divergence discussed in § 3.4 can easily dominate the exchange term and increase the spectral temperature. Even if velocity effects are suppressed a small κ_P may still cause the chromosphere to retreat within the star to higher temperatures and densities. Thus the observed spectrum may be much hotter than simple opacity arguments would predict.

3.8 Conclusions

Shock breakout is a viable means of detecting VLE SNe that would otherwise be too faint to observe, but in low-energy events care must be taken to represent the appropriate opacity processes and account for their effects on spectral temperature. This chapter details the approximations used in this model for free-free, bound-free, and bound-bound opacities. It also describes effects capable of shifting the spectral temperature of the breakout, notably velocity divergence and high absorptive opacities.

Chapter 4

FLD Simulations of Shock Breakout in Very Low Energy Supernovae

4.1 Introduction

Starting with the theoretical foundation discussed in Chapter 3, shock breakouts in VLE SNe may be studied in simulation. First the CASTRO code and its radiation module are validated for the most well-understood shock breakout case in the literature, SN1987A. Then VLE SNe models in red supergiants are simulated in CASTRO. Although analytic estimates of VLE breakout exist (Piro, 2013), no numerical simulations have yet been carried out. In particular the color temperature T_c, which is distinct from the effective temperature T_e, has not been calculated in VLE SNe because its determination requires a multigroup treatment of radiation. In the coming age of large-scale transient surveys accurate light curves and spectra will be vital for mission planning and analysis. Without such models, these transients might easily be confused with other phenomena having similar time scales and luminosities - for instance, novae, failed Type Ia SNe, tidal disruption events, or common envelope ejection from binary mergers - and the light curve automated selection criteria can inadvertently misclassify interesting transients or even ignore them altogether. Template light curves and spectra of VLE SNe breakouts are therefore provided in the hopes of guiding observation.

4.2 Verification and Validation of CASTRO: SN1987A

Because CASTRO's MGFLD module is new, it is important to first verify its capabilities for this sort of simulation. A frequently modeled shock breakout event is that of SN1987A, which has been previously simulated by Ensman and Burrows (1992) (EB92) with the VISPHOT code and Tolstov *et al.* (2013) (T12) in 2012 with the STELLA code. SN1987A also has upper limits on the temperature and luminosity of its shock breakout that were derived after the fact from observations of the ionization of the surrounding gas (Fransson *et al.*, 1989; Lundqvist and Fransson, 1996). The progenitor chosen was an 18 $M_{\odot}$ blue supergiant with a radius of 3.2×10^{12} cm, shown in Figure 4.1, the same model studied in EB92. This model was also studied in Sukhbold *et al.* (2015). Two different explosion energies were sampled. One model at 1.0 B was close to the observed value, near 1.3×10^{51} erg (Arnett *et al.*, 1989) and the other model at 2.3 B, was chosen to match the second simulation in EB92. The high temperatures in SN1987A's breakout ensure that electron scattering opacity is dominant.

The 1.0 B progenitor was simulated in both single-group (grey radiation) and multigroup mode; the 2.3 B progenitor was studied only in single-group. The results are shown in Figure 4.2 which gives the bolometric light curve, and Figure 4.3 which gives the spectrum at peak T_c. Peak

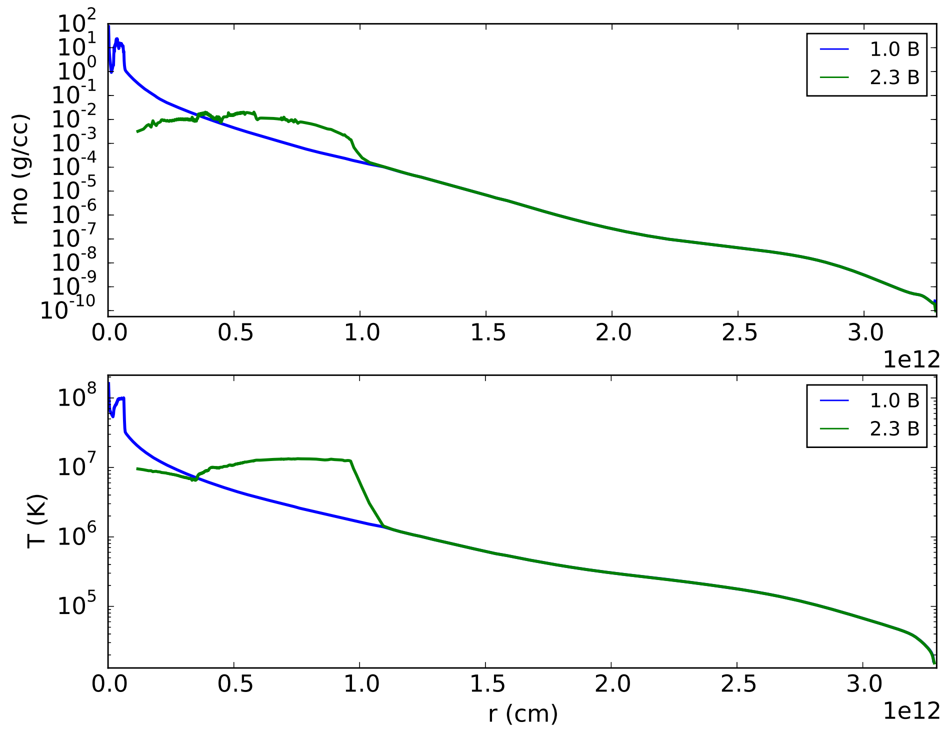

Figure 4.1: Density and temperature profiles for the SN1987A progenitor at the time the calculation was linked from the KEPLER code to CASTRO for two different explosion energies, 1.0 B (blue) and 2.3 B (green).

Table 4.1: SN1987A Breakout Model Results

Model	Star	v^a(km/s)	KE^b(ergs)	L_{peak} (erg/s)	Δt^c(s)	Max T_e (K)	Max T_c (K)
1.0 B	SN1987A	2.0×10^4	1.08×10^{51}	6.77×10^{44}	70.7	5.13×10^5	1.1×10^6
2.3 B	SN1987A	3.2×10^4	2.01×10^{51}	1.53×10^{45}	45.0	6.29×10^5	$\cdots$

[a]Velocity at breakout.

[b]Kinetic energy at breakout.

[c]Full-width half-max of travel-time-corrected light curve.

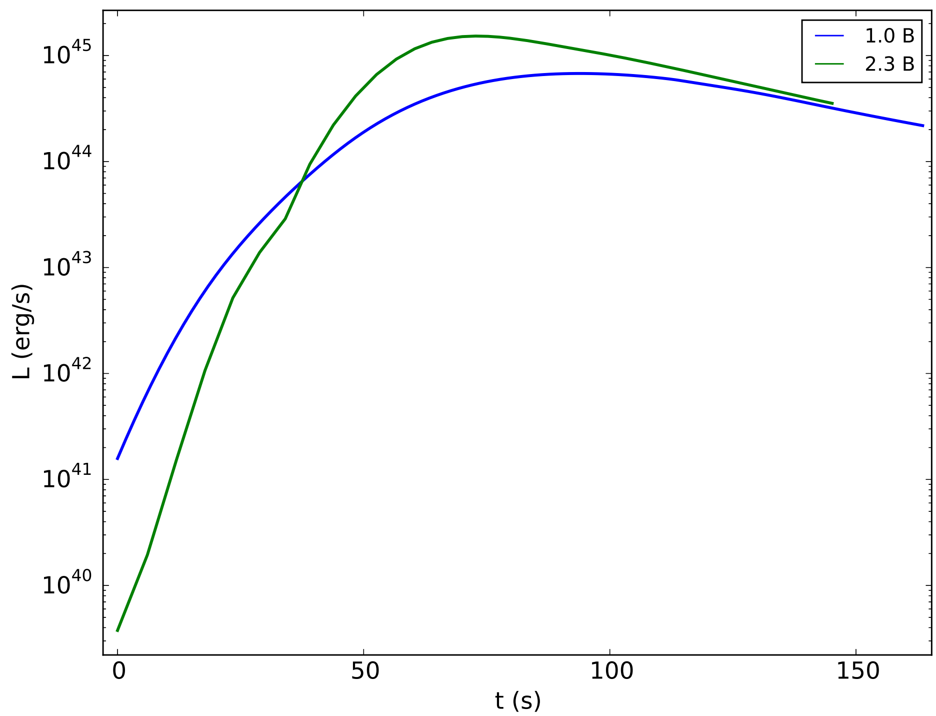

Figure 4.2: Bolometric light curves for shock breakout in SN1987A calculated for two different explosion energies using CASTRO, 1.0 B (blue) and 2.3 B (green). The higher-energy breakout is significantly brighter and shorter. The curves have been arbitrarily shifted in time to overlay at peak for ease of comparison.

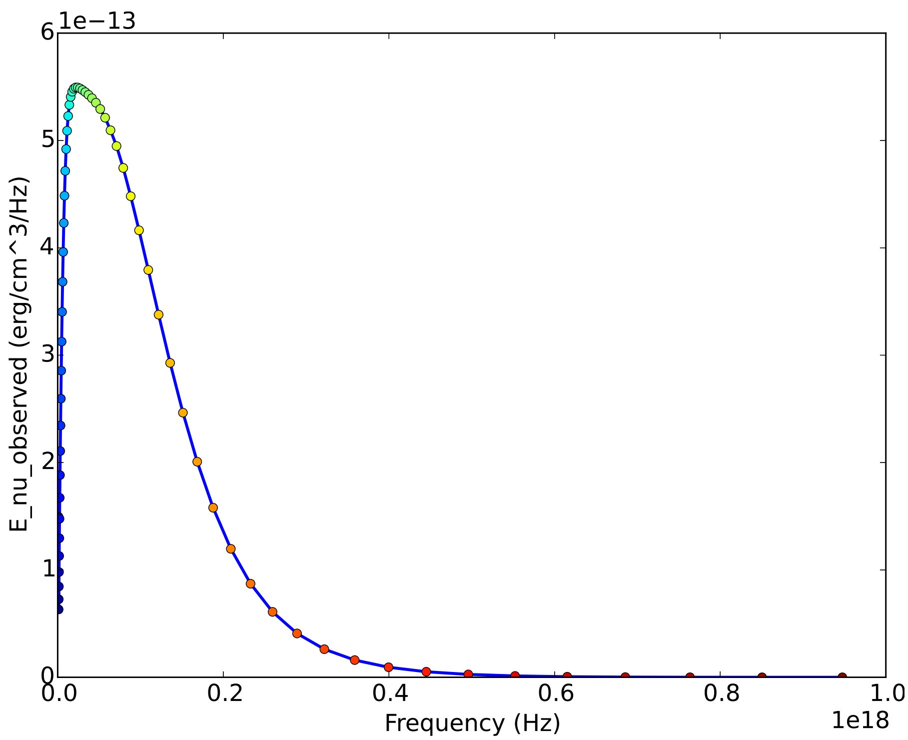

Figure 4.3: Spectrum for shock breakout in SN1987A for a 1.0 B explosion calculated using CASTRO and sampled at peak color temperature. Circles mark the centers of frequency groups. Sixty-four groups were used in this calculation. This spectrum has a blackbody form and an effective temperature of $T_e = 5.41 \times 10^5$ K, but applying Wien's Law to the peak frequency gives a color temperature $T_c = 1.1 \times 10^6$ K.

Table 4.2: Presupernova Star Parameters

Star	Final Mass ($M_\odot$)	He Core Mass ($M_\odot$)	Radius (cm)
SN1987A	15	8	3.2×10^{13}
RSG15	12.79	4.27	6×10^{13}
RSG25	15.84	8.20	1.07×10^{14}

T_c will occur near the very beginning of the breakout, while the bolometric luminosity will rise on a longer timescale; in SN1987A the peak luminosity occurs about 100 seconds after peak color temperature. Bremsstrahlung and photoionization opacities are negligible in this energy regime and are not included. Comptonization is included and the ratio κ_P/χ_R has been set to 5×10^{-3} in order to ensure the source exchange term is dominant (§ 3.4). The bolometric light curve is similar to past studies with a luminosity that peaks around 10^{45} erg/s, indicating a high-energy explosion. The breakout light curve has a width of ~ 100 s, indicating a small stellar radius. Peak effective temperature occurs at peak luminosity, and the ratio of peak temperatures $T_c/T_e = 1.1\times10^6$ K$/5.5\times10^5$ K = 2.7, matching the theoretical prediction of a ratio between two and three. The 2.3 B explosion has a higher and sharper peak than the 1.0 B. A full summary of the results can be found in Table 4.1.

These results match both prior simulations and theoretical predictions; we can therefore be confident in CASTRO's ability to handle this problem.

4.3 Simulation Setup

4.3.1 Progenitor Stars

As discussed in § 1.2, based on a number of recent surveys (e.g., O'Connor and Ott, 2011; Pejcha and Thompson, 2015; Sukhbold *et al.*, 2015) the presupernova progenitor masses most likely to produce black holes in stars that still retain their envelopes lie in the range 15 to 35 $M_{\odot}$. Especially prolific in black hole production may be the stars 18 to 26 $M_{\odot}$(Horiuchi *et al.*, 2011; Ugliano *et al.*, 2012; Brown and Woosley, 2013a; Sukhbold and Woosley, 2014; Kochanek, 2014; Clausen *et al.*, 2015). In order to sample this range, two progenitor stars are used, both red supergiants, with masses 15 $M_{\odot}$(RSG15) and 25 $M_{\odot}$(RSG25). Their presupernova structures are shown in Figure 4.4; as these are the same two models used in Chapter 2, their detailed composition is shown in Figure 2.2 and Figure 2.3. Since the radiation produced by breakout depends chiefly on the energy, which will be varied, and the presupernova radius, which changes gradually by about a factor of two in the mass range of interest, these two models should suffice. The models here are taken from Woosley and Heger (2007) and are very similar to those more recently explored by Sukhbold and Woosley (2014) and Sukhbold *et al.* (2015).

These stars were evolved using the KEPLER code (Weaver *et al.*, 1978; Woosley *et al.*, 2002) from ignition on the main sequence to the time of collapse. An artificial shock of variable energy was initiated by first extracting the iron core and then dumping energy in the bottom 10 zones. Since the calculations here do not depend upon nucleosynthesis or details of how the explosion was powered, this approach is as good as any.

It is important to note that the energy deposited, the shock energy at the time of breakout, and the final kinetic energy at infinity of the ejecta are three different quantities. Not all energy

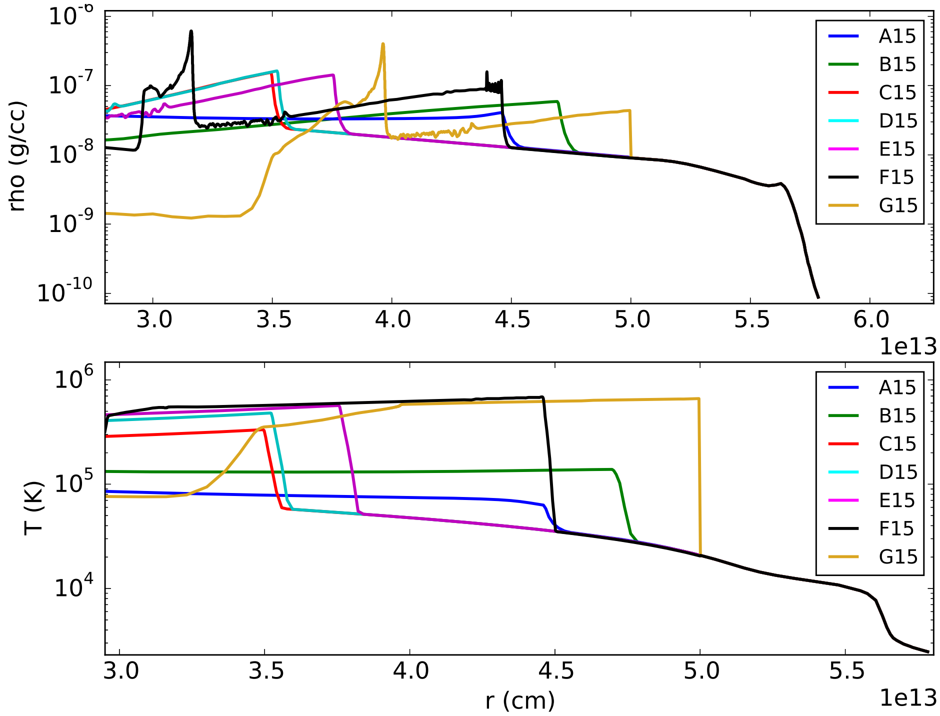

Figure 4.4: Density and temperature profiles for RSG15 at the time the calculation was linked from the KEPLER code to CASTRO for five different explosion energies. The shock energies increase alphabetically. The time, and hence radius of the link was arbitrary, but sufficiently early and deep in that the shock was still in very optically thick regions of the star. The KEPLER zoning was relatively coarse with only 40 zones external to 5×10^{13} cm. The surface structure is (or should be) unchanged since the shock wave was launched and is identical to the pre-supernova stellar atmosphere. Because of this coarse zoning and crude surface physics, the effect of using a model atmosphere was explored in § 4.3.3.

deposited becomes kinetic, and the shock energy at breakout is not the same as the total energy which includes both positive internal and negative gravitational energy. Both the kinetic energy at breakout, which is relevant for breakout, and the final kinetic energy, which is relevant for the later light curve, are given in Table 4.3.

In most core-collapse simulations, the properties of the pre-collapse stellar atmosphere are irrelevant, as it will be quickly disrupted by the explosion itself. But the crucial physics of shock breakout occur at this layer. Care must be taken to treat it accurately in shock breakout stud-

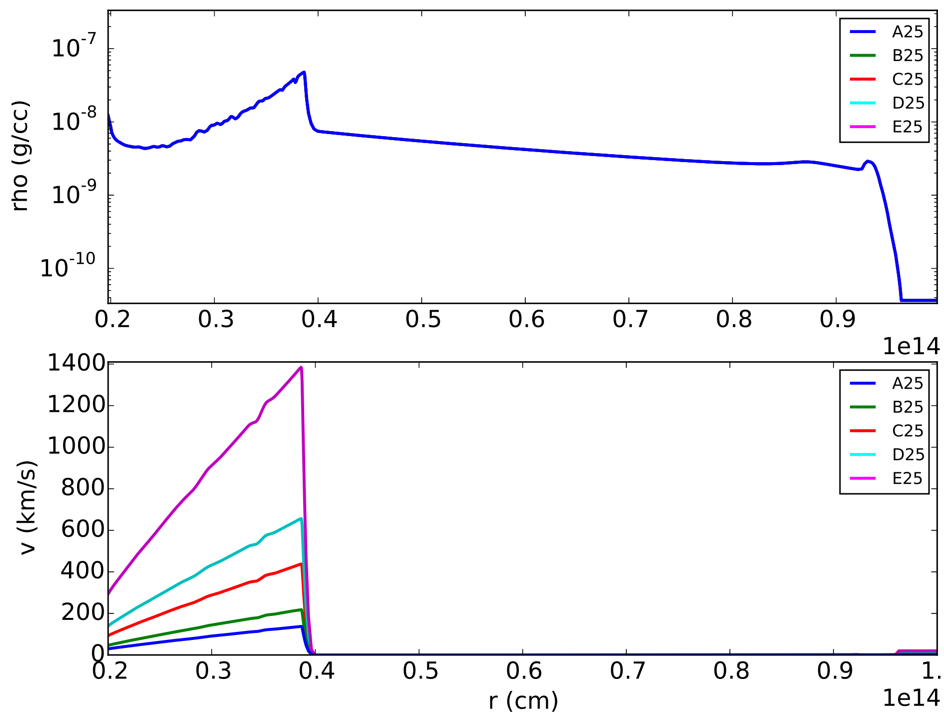

Figure 4.5: Density and velocity profiles for RSG25 at link time from KEPLER to CASTRO. RSG25 models with varying energies were produced by multiplying the velocities in a single RSG25 model (here designated C25) by a constant factor at link time. Density and temperature profiles were assumed to be the same.

ies. Additional modifications were therefore made to the progenitor models' atmospheres. These modifications are discussed in § 4.3.3.

Three calculations were then done, a refined one of breakout using CASTRO (§ 4.5); a crude one of breakout using KEPLER, and a refined calculation of the later light curve using KEPLER (§ 4.5.3). KEPLER performs only single temperature flux-limited radiation transport, but as long as the model is mapped into CASTRO at a time when the material is still very optically thick and the radiation is fully thermalized, no loss of precision occurs. Breakout in KEPLER gives information on the bolometric luminosity and effective emission temperature that is useful to compare with CASTRO. Only the CASTRO calculation gives information on the color temperature and spectrum.

Due to their large radii, breakout transients in red supergiants have a much longer time scale, and this is lengthened further by the low energies considered. Typical durations are hours to days. The much larger size also presents simulation challenges. The model atmospheres of the RSG progenitors are comparable to the size of SN1987A's entire progenitor. Resolving the red supergiants properly required the use of constant, predefined mesh refinement. One coarse grid covered the entire domain, and another refined by a factor of 4 covered the star itself.

4.3.2 Choice of Energies

Explosion energies in the range $10^{47} - 10^{50}$ ergs were explored for red supergiants. The lowest energy is set by the approximate binding energy of the hydrogen envelope. The upper bound to the energy range studied is set by the lowest energy supernovae that have already been detected. The Crab supernova for example, is thought to have had an energy of near 10^{50} erg (Yang and Chevalier, 2015). At the lower bound even the recombination of the hydrogen and helium in the envelope gives $\sim 10^{47}$ erg and it is difficult to imagine the ejection of most of the envelope with less energy. This also gives very low velocity and a long transient that might be difficult to detect or easily confused with other sources. This sort of event might result from nuclear instabilities in the core during oxygen and silicon burning. For example, the stronger silicon flash studied in stars of near 10 $M_{\odot}$by Woosley and Heger (2015) imparted a kinetic energy to the envelope of $\sim 5 \times 10^{49}$ erg, but weaker flashes imparted far less, down to a few $\times 10^{47}$ erg. Unfortunately very weak shocks did not make it to the surface before the core collapsed and a new shock was launched. A shock of 3×10^{48} erg did reach the surface though. Shiode and Quataert (2014) estimate that convection in presupernova stars can drive shocks with $10^{46} - 10^{48}$ ergs of energy. Energies of 10^{47} - 10^{48} erg were also seen in the transients studied earlier in Chapter 2. Models F15 (0.5 B) and G15 (1.2 B) are simulated for comparison purposes.

Because the energy in the shock at breakout depends only on the local velocity structure in the hydrogen envelope, additional models were generated in the CASTRO code by multiplying the velocity in the KEPLER model at link time by a variable factor. This gave greater control over the energy and allowed for a greater diversity of models to be studied. All RSG15 models were calculated individually using KEPLER. In order to have more control over the explosion energy and survey a grid of possibilities, the RSG25 models were produced by multiplying the velocities in KEPLER Model A25 by a constant factor.

4.3.3 Stellar Atmospheres

KEPLER is designed to study the internal structure and nucleosynthesis of stars and does not treat the outer stellar atmosphere very carefully. However shock breakout is fundamentally an atmospheric phenomenon, since its properties are governed by the critical thick-to-thin transition region near the photosphere. In the SN1987A models, this atmosphere is on the order of 1×10^{12} cm thick; in the RSG models it is $\sim 6 \times 10^{12}$. The effect of variations in the stellar atmosphere was tested by running two different simulations of shock breakout in SN 1987A. The first model had its atmosphere replaced by a power law fit of the form $\log_{10}\rho = \alpha_1,\ \log_{10} r + \beta_1,\ \log_{10} T = \alpha_2,\ \log_{10} r + \beta_2$, where α, β were determined by fitting the original KEPLER data. The fits gave $\alpha_1 = -42.1,\ \beta_1 = 518.0,\ \alpha_2 = -26.4,\ \beta_2 = 334.5$. The second model then had its atmosphere replaced by the same power law form using $\alpha_1/2, \alpha_2/2$, generating a significantly less steep gradient. As can be seen in Figure 4.6, the different atmospheres result in quite different breakout profiles. The two breakouts have the same integrated energy, since that energy is being released from the shockwave itself, but the more slowly varying atmosphere influences the time scale and temperature of the observed transient. A shallower atmospheric gradient creates a wider transition region and thus a breakout that is longer lasting and correspondingly less luminous at peak, while a steeper gradient creates a harder, faster transient.

The true atmosphere of SN 1987A's progenitor is not expected to vary this much between presupernova models, but this comparison does demonstrate that differences in the atmospheric gradient can produce corresponding and significant differences in the resulting light curves. KEPLER does not zone this atmosphere finely by default, and during the propagation of the shock waves from the core to the CASTRO link point, physics changes designed to simulate shock wave structure as well as possible can lead to secondary responses in the atmosphere. Since explosions at different energies take different amounts of time to reach the surface, this can also lead to variations between different models in the same pre-supernova progenitor. These divergences are clearly unphysical and modifications to the CASTRO input models are therefore required.

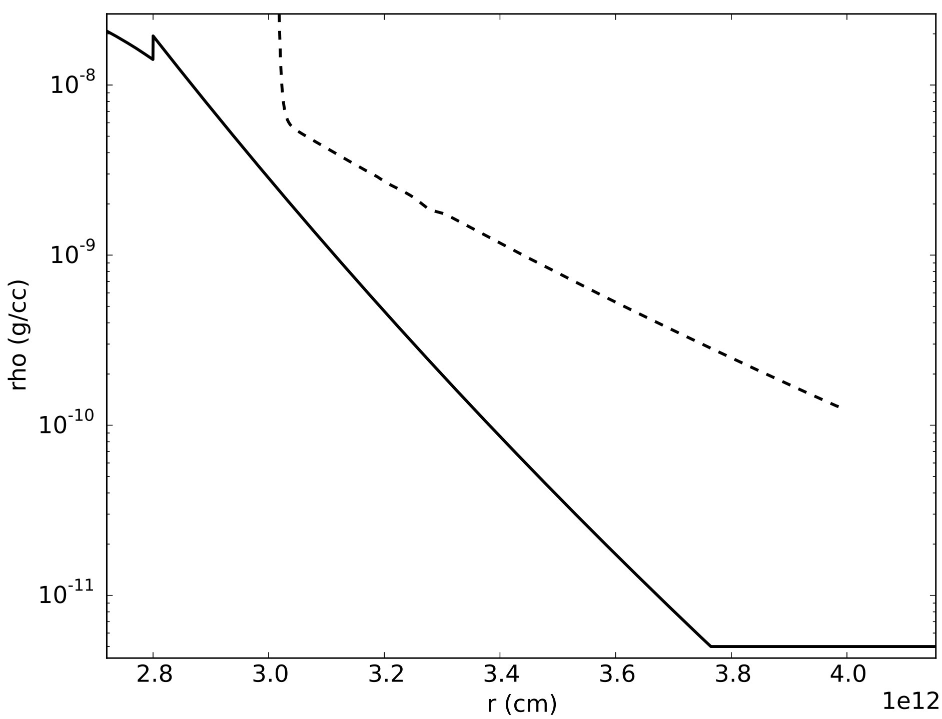

Figure 4.6: Density of SN1987A presupernova model with two different stellar atmospheres applied: a power law fit to the initial KEPLER model of the form $\rho = \alpha_1,\ \log_{10} r + \beta_1$ (solid), and the same power law fit made shallower by using $\rho = (\alpha_1/2),\ \log_{10} r + \beta_1$ (dashed).

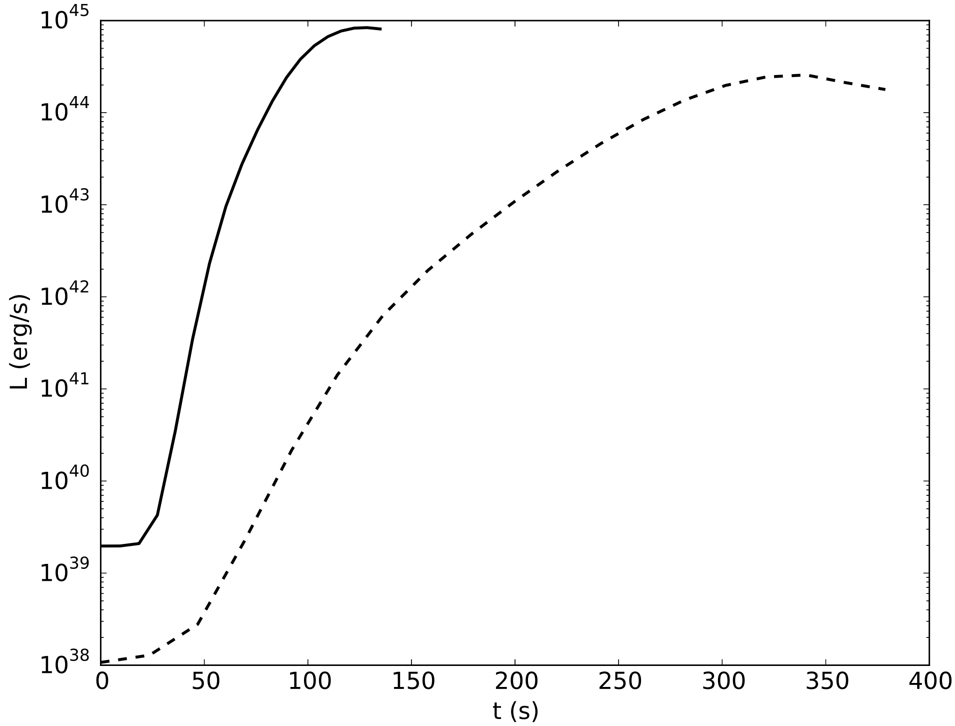

Figure 4.7: Light curves for SN 1987A breakout corresponding to the 2 different stellar atmospheres in Figure 4.6, a power law fit to the initial KEPLER model of the form $\rho = \alpha_1 \log_{10} r + \beta_1$ (solid) and a shallower gradient fit of the form $\rho = (\alpha_1/2)\log_{10} r + \beta_1$ (dashed). Despite beginning with the same shockwave, breakout through the two atmospheres is significantly different. The shallower atmosphere produces a longer and dimmer breakout than both the steeper model and comparison results from other simulations of this event. Thus differences in the atmospheric gradient can produce corresponding differences in the results, and the atmosphere must therefore be treated with care.

An alternative to a simple power-law extrapolation of the density structure in the KEPLER presupernova star's outer zones is to use a model stellar atmosphere. For the 15 $M_\odot$ red supergiant models, realistic model atmospheres were available from the MARCS database (Gustafsson, B. *et al.*, 2008). The MARCS atmospheres were calculated using a specialized code designed to help observers fit spectra for observed red supergiants. The atmospheres include NLTE effects not simulated in either KEPLER or CASTRO, as well as the effects of line blanketing. RSG15 progenitor has $T_e \sim 3550$ K, solar metallicity, and log surface gravity of -0.32. The two MARCS atmospheres closest to RSG15 were selected based upon T_e, metallicity, and log specific surface gravity, then interpolated to fit the KEPLER progenitor's properties. The MARCS atmosphere data extend approximately 5×10^{12} cm below and 1×10^{12} cm above the photosphere. In order to ensure a smooth transition a power law was fit to the combined MARCS atmosphere and KEPLER model and used to replace all RSG15 atmospheres. This replacement provided a much more accurate, consistent atmospheric gradient. The final progenitor atmospheres are shown in Figure 4.8.

The atmosphere of a 25 $M_\odot$red supergiant is more complex and has been less well-studied in simulation. This progenitor's envelope is very extended and loosely bound. Once the star reaches this stage of its life it will have likely lost part or all of the envelope to winds or other instabilities and uncertainties in mass loss make it difficult to estimate the atmosphere's structure. The section of parameter space explored by MARCS did not extend near enough to our progenitor star to reliably extrapolate the data. Thus for RSG25 a power law of the same form as the 87A fit described above is fit to the existing KEPLER model and used to replace the progenitor atmospheres.

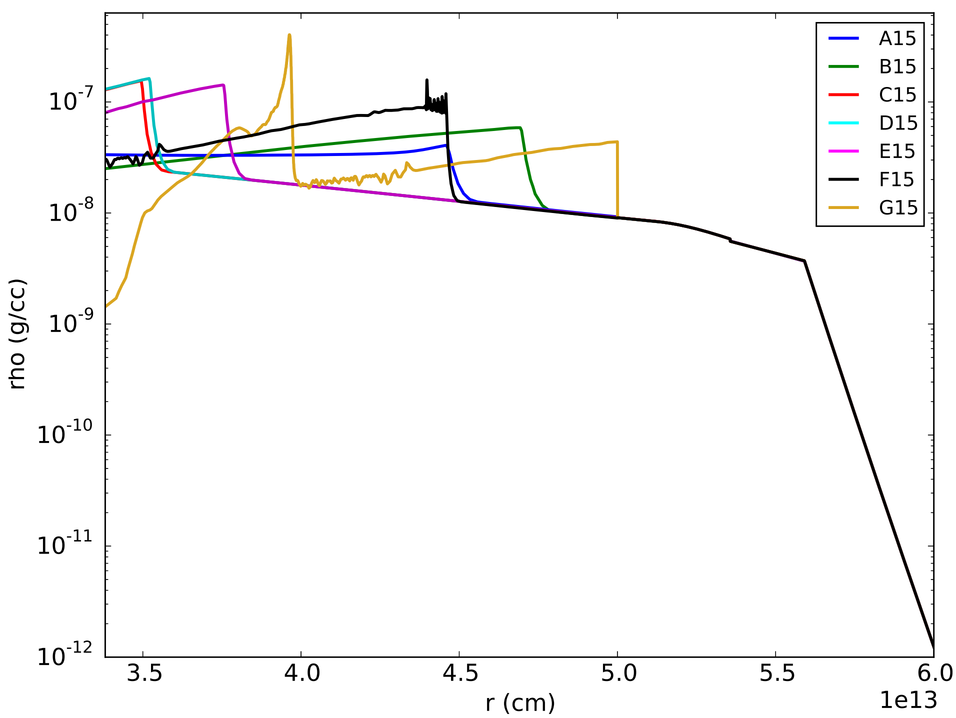

Figure 4.8: Density profiles for the 5 RSG15 presupernova models from Figure 4.4, revised with MARCS model atmosphere in place of original KEPLER atmosphere.

4.3.4 Equation of State and Network

These models used an 18-species network, terminating at nickel, with two auxiliary variables, electron fraction Y_e and mean molecular mass $1/\mu$. Nuclear reactions are turned off and all species are passively advected. In the regions of interest the composition is overwhelmingly dominated by hydrogen and helium at relatively low temperatures, so an ideal gas law plus radiation provides an accurate equation of state. KEPLER has its own general equation of state that is good under all conditions except extremely high density. There was good agreement between the KEPLER pressure, internal energy, temperature and density and the equivalent quantities in CASTRO after the remap.

4.3.5 Opacity

As discussed in Chapter 3, shock breakout is fundamentally a transition of the shock wave from an optically-thick to optically-thin region, and an accurate treatment of opacity is critical to obtaining realistic results. The crucial physics of shock breakout occurs at and behind the shock front where the gas temperature is in the range 4.5×10^4 - 1×10^6 K when breakout occurs, depending on the model's energy. In this regime, the scattering opacity is dominated by Thomson scattering, which can be easily calculated using the free electron density from a Saha solver. Scattering easily dominates total opacity in all our models, electron scattering easily dominates total scattering, and our H-He Saha solver gives a precise value for the electron density. This gives reliable estimates of parameters that depend only on total opacity, such as radius of the stellar photosphere and overall shape of the bolometric light curve. The absorptive opacity is more complex. Both free-free and bound-free (photoionization) processes contribute, as well as the effective absorption arising from energy losses during inelastic electron scattering.

For each time step in the simulations, the Saha equation was solved assuming the presence of only hydrogen and helium. At the relevant temperatures and mass fractions this is a good approximation. The electron abundance is then used to calculate both a total opacity χ_R (assumed to be dominated by scattering) and a small contribution to absorptive opacity $\kappa_{P\,c}$, computed by assuming a fixed ratio $\epsilon = \kappa_{P\,c}/\chi_R$. Both Thomson scattering and its contribution to absorptive opacity are grey i.e. insensitive to frequency. Inverse bremsstrahlung absorption is calculated according to the equations discussed in § 3.5.1. Photoionization absorption contributed by metals is calculated according to the equations discussed in § 3.5.2. Line opacities, bremsstrahlung processes below 4.5×10^4 K, and photoionization processes below 4.5×10^4 K are not accounted-for, as the former requires much more detailed calculations (§ 3.5.3) and the grey opacity laws for the latter two processes break down once their assumptions of complete H and He ionization are violated. For details on both the theory and implementation of these opacities, see § 3.5.

CASTRO is an Eulerian code and thus requires a certain amount of mass in every cell on the grid, or severe instabilities will result. A very thin ambient medium is therefore placed around the progenitor star to keep it stable while the processes of interest run. In the case of shock breakout this ambient medium must be made optically thin to ensure that its presence does not distort the resulting lightcurves. The ambient medium is generally made as cold and thin as possible while still maintaining numerical stability, to avoid affecting simulation results. Photoionization opacity in this medium presents an interesting problem. Material below 4.5×10^4 K has significantly higher photoionization opacities as a greater fraction of H and He atoms are neutral, and a breakout flash entering an ambient medium at such temperatures could falsely lose a great deal of energy to ionizing its surroundings. Near the end of its life a massive star is pouring out sufficient luminosity that hydrogen and helium in the region immediately surrounding it (less than one stellar radius from the surface) should be ionized already.

4.4 Light Curves, Spectra, and Post-Processing

Light curves and spectra are evaluated by sampling the flux in a single distant cell, representing the observer. The measured flux is corrected from the comoving frame back to the lab frame, and then the entire light curve corrected for light travel time. Because of the star's curvature, a distant observer will not see the breakout front erupting uniformly across the star; rather, more distant portions of the disk will light up at later times since the light must travel slightly farther to reach the observer. The comparatively small (3×10^{12} cm) SN1987A progenitor has a light travel time of only 100 seconds, but RSG15 ($\sim6\times10^{13}$ cm) and RSG25 ($\sim1\times10^{14}$ cm) have light travel times of 2000 and nearly 10000 seconds, respectively. The overall effect of this correction is to smear the light curve out in time, increasing peak width and lowering peak brightness. We use the same simple light travel correction formula as T12:

$$L_{obs}(t) = 2\int_0^1 L(t-\tau)x\,dx, \tau = (R_p/c)(1-x)$$

This formula makes three assumptions: that the distance to the observer is large, that the radiation is isotropic, and that the photospheric radius R_p remains stationary. The first two assumptions are easily satisfied. The third is less accurate at later times as the envelope begins to expand, but the speed of the photosphere is much smaller than the speed of light and R_p can be effectively taken as constant during the light crossing time.

Spectra are calculated by sampling the individual group fluxes in the same cell as the light curve. All multigroup models in this paper were run with 64 logarithmically-spaced groups. The red supergiants were run with a frequency range $1.5 \times 10^{14} - 1 \times 10^{17}$ Hz except in the very-low-energy model A15, which was run with the frequency range $1.5 \times 10^{14} - 1 \times 10^{16}$ Hz. SN1987A was run with the range $1 \times 10^{15} - 1 \times 10^{18}$ Hz. CASTRO automatically places any energy at frequencies below the the lower limit in the lowest group, and any at frequencies higher than the upper limit in the highest group; thus a failure to resolve the correct spectral range can be detected by checking for anomalously high energies in the lowest or highest group. T_c is calculated by applying Wien's Law to the frequency group with the highest energy. T_e is calculated from the bolometric radiation flux using the standard $F = \sigma_{SB} T_e{}^4$ blackbody relation. We considered breakout to be complete when the bolometric light curve had declined to at least half of peak brightness.

4.5 Breakout in Red Supergiants: Results

In RSG15, the supernova fails almost completely at some of the lower energies. Only a small fraction of the envelope achieves escape speed, as shown in Figure 4.11. For others the envelope is ejected, but not the helium core. Bolometric light curves for RSG15 are shown in Figure 4.9. The wide range of kinetic energies examined results in a diverse set of peak luminosities. Perhaps unfortunate for their detection, duration and peak brightness are inversely related - that is, the brighter the breakout, the shorter it will likely be. Full-width half-maximum durations range from 3 h to 70 h.

Though mass loss leaves RSG15 and RSG25 with similar presupernova masses (12.79

$M_\odot$ vs. 15.84 $M_\odot$), the radius of RSG25 is nearly double the radius of RSG15. Breakouts with similar energies are thus expected to have longer light curves and lower peak energies in RSG25. Bolometric light curves (Figure 4.10) show peak luminosities around 10^{42} erg/s and durations in the 25 - 70 h range, excepting E25, whose kinetic energy at breakout was significantly higher.

Both RSG15 and RSG25 show minor anomalies in their light curves post-peak. RSG15's shock breakouts show a curious change in decline rate post-peak - initially declining quite steeply, then changing to a shallower slope. Four of RSG15's breakouts display this anomaly, and it is correspondingly extended in the longer-duration light curves. RSG25 shows a similar variation post-peak, although in this case it shows multiple peaks/changes in the rate of decline. None of these small features represent significant variations relative to the light curve of each breakout, but the fact that they appear in all light curves of a single progenitor merits further investigation. It is unclear what physical behavior causes these anomalies, but their appearance seems to be related to the formation of a high-density spike at the photosphere as the hydrodynamic shock begins to move out through the former photosphere. This spike is likely an artifact of 1D simulation and would in reality be quickly broken up by fluid instabilities. As noted, none of these features are significant relative to the overall light curves, so they can be neglected.

4.5.1 Color Temperature

As discussed in detail in § 3.6, the opacities in low-energy shock breakouts differ from those expected in standard CCSNe, as the lower temperatures bring different opacity processes into play. The total opacity in VLE SN breakout is dominated by electron scattering, but the absorption is dominated by inverse bremsstrahlung, with significant contributions from photoionization. If only Compton scattering were considered in calculating absorptive opacity, the color temperature

Table 4.3: VLE Breakout Model Results

Model	v^{a}(km/s)	$KE_b{}^{b}$(ergs)	$KE_f{}^{c}$(ergs)	L_p (erg/s)	$L_{cr}{}^{d}$(erg/s)	Δt^{e}(h)	Max T_e (K)
A15	80	3.86×10^{46}	6.58×10^{46}	9.50×10^{39}	9.57×10^{39}	68.4	8.15×10^{3}
B15	150	6.43×10^{47}	1.54×10^{48}	3.89×10^{41}	3.82×10^{41}	35.2	2.06×10^{4}
C15	320	4.98×10^{48}	1.21×10^{49}	8.39×10^{42}	8.33×10^{42}	8.1	4.44×10^{4}
D15	650	2.13×10^{49}	5.04×10^{49}	5.43×10^{43}	5.38×10^{43}	5.3	7.08×10^{4}
E15	1200	5.43×10^{49}	1.23×10^{50}	2.13×10^{44}	2.02×10^{44}	3.1	9.97×10^{4}
F15	1920	2.16×10^{50}	5.07×10^{50}	8.25×10^{44}	8.07×10^{44}	1.83	1.40×10^{5}
G15	2400	2.54×10^{50}	1.20×10^{51}	1.68×10^{45}	1.66×10^{45}	1.42	1.67×10^{5}
A25	150	1.38×10^{48}	...	9.07×10^{41}	9.03×10^{41}	67.0	1.57×10^{4}
B25	179	1.53×10^{48}	...	1.23×10^{42}	1.23×10^{42}	57.9	1.70×10^{4}
C25	210	2.27×10^{48}	6.12×10^{48}	2.76×10^{42}	2.77×10^{42}	37.0	2.08×10^{4}
D25	280	3.52×10^{48}	...	5.85×10^{42}	5.83×10^{42}	25.9	2.51×10^{4}
E25	480	1.10×10^{49}	...	3.67×10^{43}	3.61×10^{43}	9.3	3.97×10^{4}

[a]Velocity at breakout.

[b]Kinetic energy at breakout.

[c]Final kinetic energy of supernova.

[d]Corrected for light travel time.

[e]Full-width half-max of travel-time-corrected light curve.

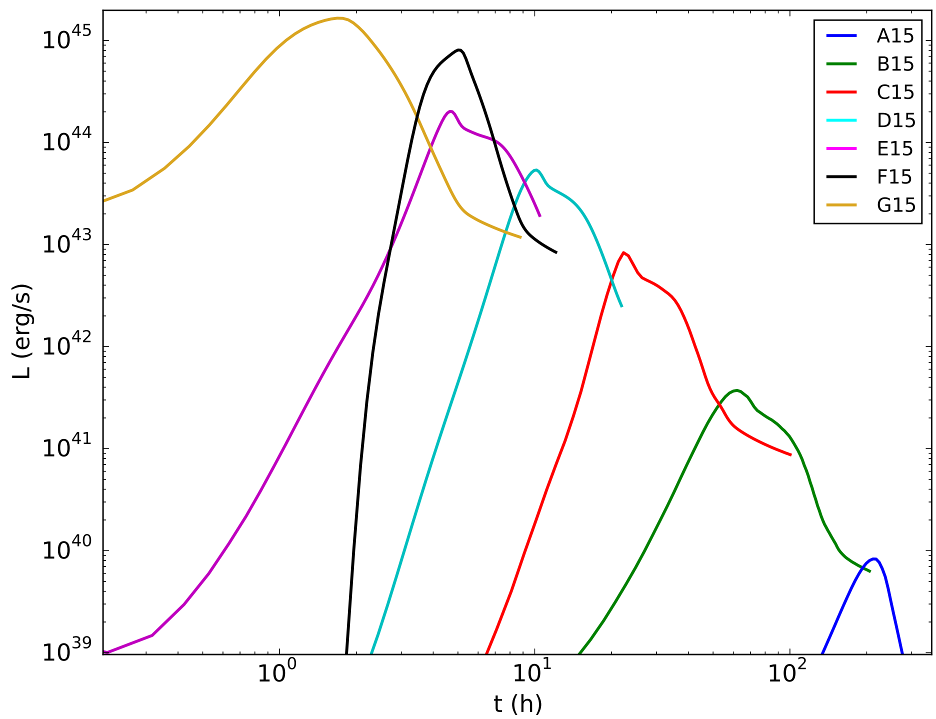

Figure 4.9: Bolometric light curves for RSG15 shock breakouts at 7 different explosion energies ranging from 3.86×10^{46} (A15) to 1.2×10^{51} (G15), calculated by CASTRO. Both peak luminosity and breakout flash duration show clear and significant variations with explosion energy. The slight anomalies in the light curve post-peak are discussed in § 4.5.

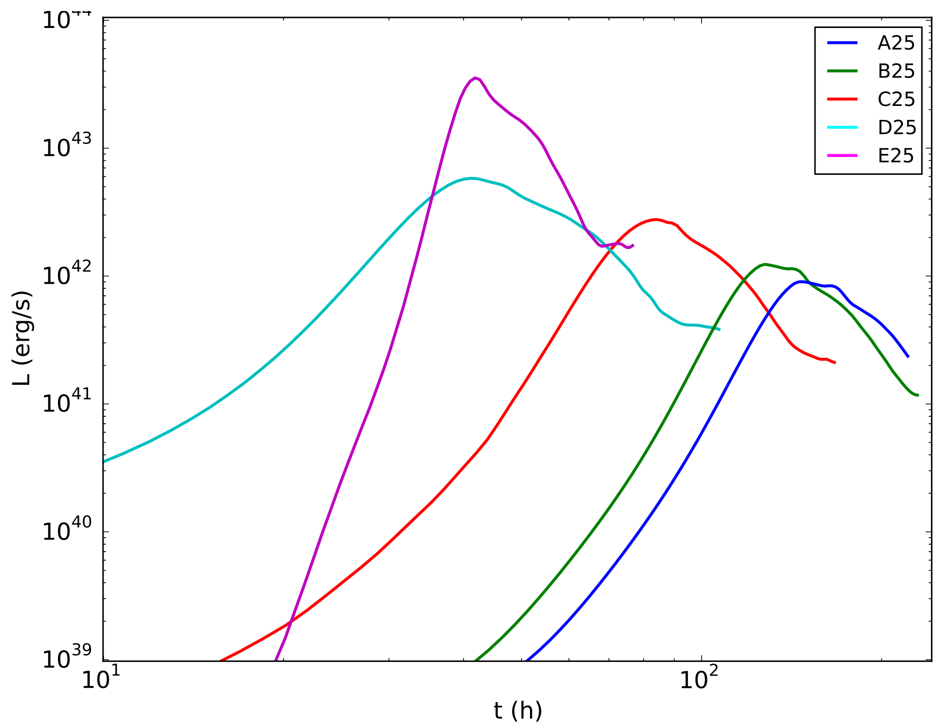

Figure 4.10: Bolometric light curves for RSG25 shock breakouts at 5 different explosion energies ranging from 1.38×10^{48} (A25) to 1.10×10^{49} (E25), calculated by CASTRO.

is expected to rise significantly above the effective temperature (§ 3.5) as the temperature drops. However inverse bremsstrahlung is expected to increase much faster than Compton scattering efficiency drops. In this case the color temperature is therefore expected to approach the effective temperature as the kinetic energy drops. When absorption opacity approaches scattering opacity, the chromosphere and photosphere will converge. As calculated in § 3.6, in SN1987A, the highest ratio between absorptive depth and total depth is about 0.01. In G15, it is 0.04. But in E15 (10^{50} erg) it is 0.5, and in B15 (10^{48} erg) it is as high as 0.7. Thus T_c and T_e are expected to converge in these models. This results in a breakout even brighter in the IR and optical windows than would be expected. The observational impacts of this effect are discussed in § 5.1.

4.5.2 Comparison to Analytic Results

Analytic predictions for shock breakout in "normal" Type IIp supernovae already exist in the literature (Tominaga *et al.*, 2011; Matzner and McKee, 1999; Katz *et al.*, 2010). Piro (2013) extended these formulas to consider the specific case of low-energy supernovae. These formulas predict the bolometric luminosity and timescale of breakouts based on the properties of the progenitor star and the explosion and can be tested against our numerical results. Piro (2013) gives:

$$L_{bo} = 1.4 \times 10^{41} \frac{E_{48}^{1.36}}{\kappa_{0.34}^{0.29} M_{10}^{0.65} R_{1000}^{0.42}} \left(\frac{\rho_1}{\rho_*}\right)^{0.194} \text{erg/s}$$

$$T_{obs} = 1.4 \times 10^{4} \frac{E_{48}^{0.34}}{\kappa_{0.34}^{0.068} M_{10}^{0.16} R_{1000}^{0.61}} \left(\frac{\rho_1}{\rho_*}\right)^{0.049} \text{K}$$

where $E_{48} = E_{kin}/10^{48}, M_{10} = M_{ej}/10\mathrm{M}_{\odot}, R_{1000} = R_*/1000R_{\odot}$, and $\kappa_{0.34} = \kappa/0.34$. Stellar radii are given in Table 4.2. It is assumed in both cases that the ejecta mass M_{ej} is equal to the size of the hydrogen envelope, that the adiabatic index $\gamma = 5/3$, and that the factor $(\rho_1/\rho_*) \sim 1$. The results are shown in Table 4.4.

There is some ambiguity in the equations as to when the quantity E_{48} should be measured; the kinetic energy at breakout will differ from the ejecta's final kinetic energy at infinity. For RSG15, the peak luminosity predictions fell much closer to the KEPLER and CASTRO results when E_{48} was assumed to be kinetic energy at infinity as measured in KEPLER. The analytic predictions and the KEPLER results are very close and both slightly underestimate the CASTRO luminosities. RSG25 shows much greater variance. The analytic predictions underestimate the numerical results by a factor of 4 - 10, with the inaccuracies increasing with kinetic energy. The analytic formulas therefore give reasonable if not precise estimates for a breakout's brightness.

4.5.3 Comparison to KEPLER Results

Figure 4.11 shows the evolution of the 5 RSG15 models post-shock breakout as simulated by KEPLER. Their plateau durations vary significantly with energy, as might be expected, but even the shortest is well over 100 days. Plateau magnitudes tend to be some 1.5 - 2 orders of magnitude lower than the breakout peak. KEPLER slightly underestimates the peak luminosity of the CASTRO breakouts; its results fall within a factor of 1 - 3 of the analytic predictions. Full results are shown in Table 4.4 and Table 4.5.

As noted in Section § 4.3.1, the model atmospheres were replaced in the move from KEPLER to CASTRO. Fig. 4.13 shows bolometric luminosity of a CASTRO breakout using the MARCS atmosphere compared to a CASTRO breakout using a fitted version of the original KEPLER atmosphere only. The differences are slight but present, but finer zoning in KEPLER's atmosphere reduces this inaccuracy. KEPLER of course cannot compute a color temperature, so we cannot compare that result directly to CASTRO's.

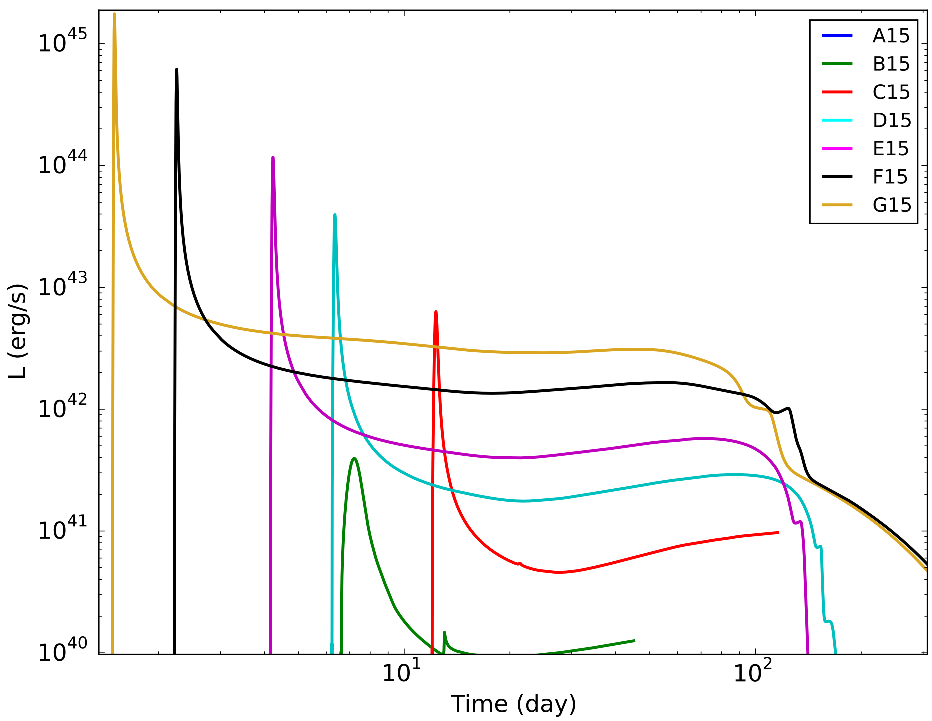

Figure 4.11: Late-time light curves calculated by KEPLER showing the evolution and plateau phase of RSG15 models. Calculations assumed opacity due to electron scattering and an opacity floor of 10^{-5} cm^2 g^{-1}.

Table 4.4: CASTRO Comparison to Other Models

Model	KE_f[a] (ergs)	L_{peak} (erg/s)	Pred. L (erg/s)	Max T_e (K)	Pred. T_e (K)
A15	6.58×10^{46}	9.50×10^{39}	4.25×10^{39}	8.15×10^{3}	6.29×10^{3}
B15	1.54×10^{48}	3.89×10^{41}	3.10×10^{41}	2.06×10^{4}	1.84×10^{4}
C15	1.21×10^{49}	8.31×10^{42}	5.11×10^{42}	4.44×10^{4}	3.71×10^{4}
D15	5.04×10^{49}	5.43×10^{43}	3.56×10^{43}	7.08×10^{4}	6.02×10^{4}
E15	1.23×10^{50}	2.13×10^{44}	1.20×10^{44}	9.97×10^{4}	8.15×10^{4}
F15	5.07×10^{50}	8.25×10^{44}	8.06×10^{44}	1.40×10^{5}	1.31×10^{5}
G15	1.20×10^{51}	1.68×10^{45}	2.65×10^{45}	1.67×10^{5}	1.77×10^{5}

[a]Final kinetic energy as measured in KEPLER

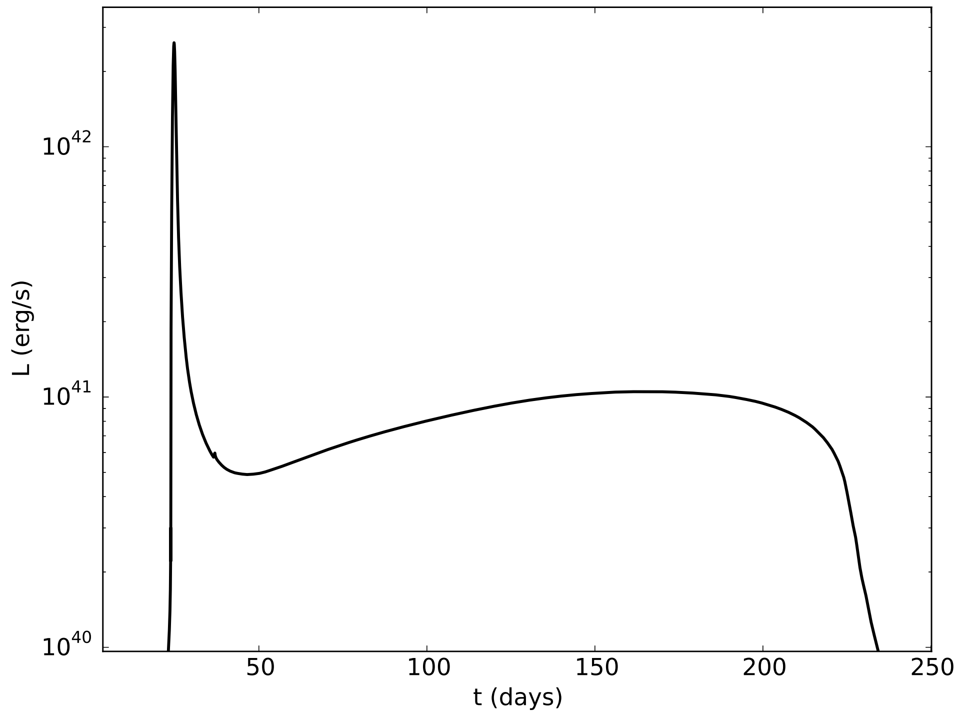

Figure 4.12: Late-time light curve calculated by KEPLER for the RSG25 models.

Table 4.5: KEPLER Comparison to Other Models

Model	KE_f[a] (ergs)	L_K[b] (erg/s)	Pred. L (erg/s)	$T_{e,K}$[c] (K)	Pred. T_e (K)
A15	6.58×10^{46}	5.09×10^{39}	4.25×10^{39}	6.93×10^{3}	6.29×10^{3}
B15	1.54×10^{48}	3.94×10^{41}	3.10×10^{41}	1.99×10^{4}	1.84×10^{4}
C15	1.21×10^{49}	6.32×10^{42}	5.11×10^{42}	4.02×10^{4}	3.71×10^{4}
D15	5.04×10^{49}	3.95×10^{43}	3.56×10^{43}	6.36×10^{4}	6.02×10^{4}
E15	1.23×10^{50}	1.17×10^{44}	1.20×10^{44}	8.34×10^{4}	8.15×10^{4}
F15	5.07×10^{50}	6.17×10^{44}	8.06×10^{44}	1.30×10^{5}	1.31×10^{5}
G15	1.20×10^{51}	1.76×10^{45}	2.65×10^{45}	1.69×10^{5}	1.77×10^{5}

[a] Final kinetic energy as measured in KEPLER

[b] Peak luminosity of light curve in KEPLER.

[c] Peak effective temperature in KEPLER.

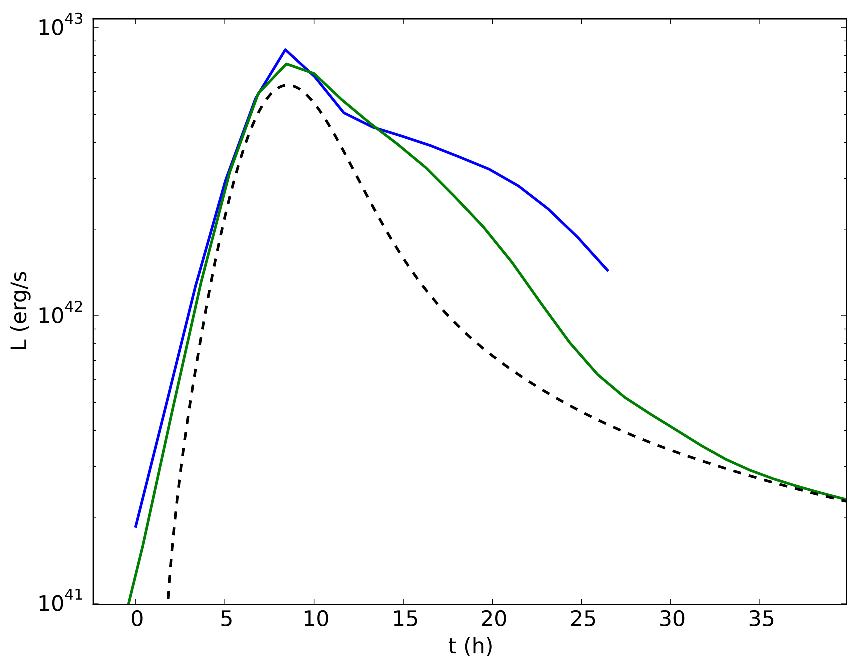

Figure 4.13: Light curves for breakout in RSG15, model C15, calculated in CASTRO for 2 different stellar atmospheres: MARCS fit (blue); and fit to initial KEPLER data (green). The dashed line shows the light curve for the same model as computed entirely in KEPLER with fine zoning.

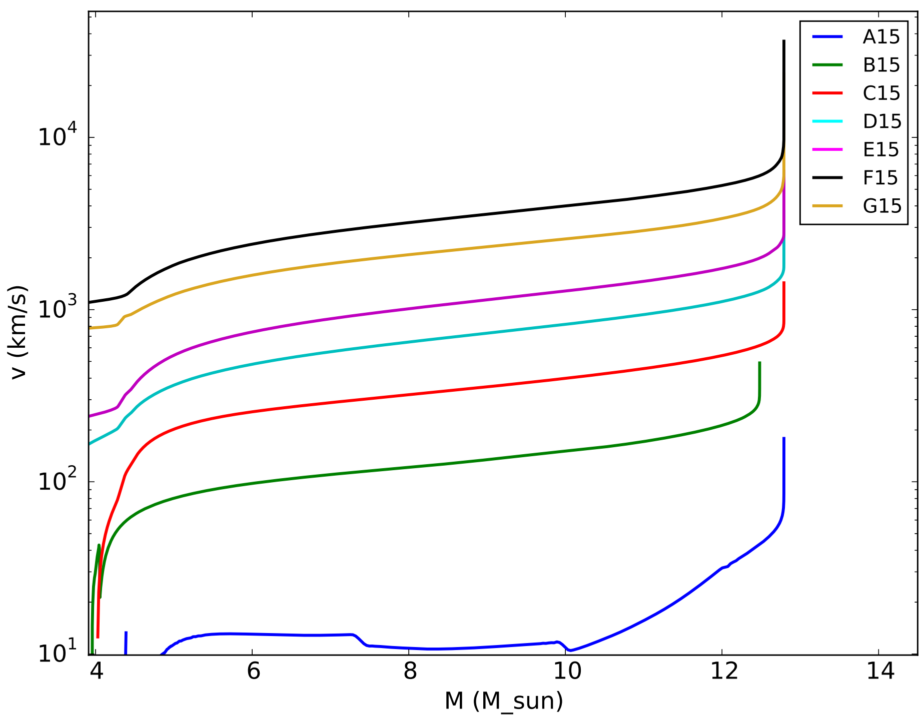

Figure 4.14: Late-time velocity profiles as calculated by KEPLER for RSG15 models.

4.6 Conclusions

Observing supernova shock breakout represents a promising method for both detecting otherwise dim supernova and retrieving information about their progenitor stars. Shock breakouts in VLE SNe in particular are easier to observe than those in regular CCSNe because of their extended duration, and are easier to observe than their associated SN because of their higher luminosity. In red supergiants the effective temperature of the breakout places the bulk of the emission in the hard UV bands rather than the X-ray, making them easier to observe with existing instruments. These considerations will be discussed further in Chapter 5.

The shock breakout of SN1987A is modeled first as a test of the CASTRO multigroup radiation transport module. These simulations give peak luminosities, durations, and color temperatures comparable to other published SN1987A breakout results. A range of low-energy explosions are then modeled in two red supergiants, RSG15 and RSG25, bracketing the suspected mass range of failed supernovae. These events give light curves and spectra that show clear variations with both explosion energy and progenitor radius. Peak bolometric luminosities range from $10^{39} - 10^{43}$ erg/s and spectral temperatures range from 4.43×10^4 - 4.78×10^5 depending on explosion energy and progenitor mass. Analytic solutions tested against these numerical results provide reasonable approximations of the results.

Chapter 5

Observing Prospects and Candidate Events

The most realistic and refined simulations are still of little use without observations to test them. Current and near-future surveys are discussed as well as recovered candidates for VLE SNe and CCSNe failures. Considerations and guidance for future observations of the transients discussed in this dissertation are also provided, especially with regard to the expected color temperatures in VLE SNe as opposed to standard-energy breakouts.

5.1 VLE SNe Breakout in Optical & IR

The reported detections of shock breakout by the Kepler satellite (Garnavich *et al.*, 2016), which observes primarily in the optical and near-infrared, raise a point of particular interest to VLE SNe: the color temperatures of these faint breakouts are significantly cooler than those of more energetic events, both because of their lower shock energies and because of the convergence of T_c

and T_e as discussed in § 3.6. Although the bolometric luminosity of these events is much lower than normal CCSNe, more of the energy will be emitted at low frequencies. Thus in an IR band the low-energy breakout may actually appear *brighter* than its more energetic counterpart, and will have greater total energy.

A simple estimate of the brightness of breakout transients in any given band can be found by assuming the spectrum is a blackbody at T_c and calculating the fraction of blackbody energy inside that bandpass. More accurate calculations would be done using a measured filter curve. The Kepler satellite has an IR bandpass of 0.4 - 0.9 microns. Fig. 5.1 shows the results of calculating the fraction of blackbody energy emitted within that bandpass, assuming that $T_c = T_e$ in low-energy events. The dynamic range of peak luminosities is significantly compressed, as the brighter breakouts also have higher color temperatures. However the duration of the transient is unaffected, and thus breakout events of similar luminosity can still be distinguished in energy by measuring the duration. The peak luminosities for these filtered curves range from 4×10^{41} - 4×10^{39} erg/s, meaning that these are still dim events, but not out of reach of current and future surveys; notably, they are significantly brighter for longer than a standard-energy breakout.

5.2 UV Extinction

Red supergiant breakouts may be cooler than those from more compact stars, but they still emit the bulk of their energy in the hard UV. Light emitted at frequencies higher than the Lyman α limit = 1216 Å has a good chance of being absorbed and at a color temperature 1×10^5 K approximately 95% of light is emitted above this limit. Since these transients are already faint, nearby (z $\ll$ 1) events are already the primary target, and the majority of absorption will occur

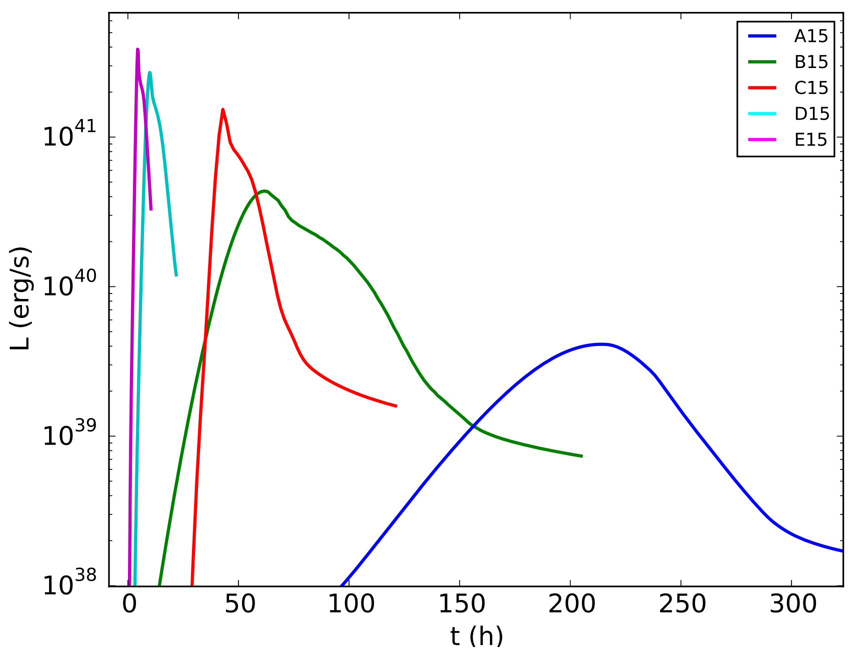

Figure 5.1: RSG15 models as they would be observed in the band 0.4 - 0.9 microns. Higher-energy breakouts have greater bolometric luminosity, but also have higher color temperature; these effects combine to suppress the peak luminosity of higher-energy models more than lower-energy models. Duration remains unaffected.

either at the source or in the Galaxy. The UV attenuation will therefore depend on the viewing angle through the Galaxy and the unknown circumstellar medium at the source. The hard UV band is not accessible with ground-based telescopes, but redshift may bring breakout spectra down into optical windows.

5.3 Searches for Failed Supernovae

Kochanek *et al.* (2008) proposed to begin a novel search for completely failed CCSNe by looking not for the presence but for the absence of sources. The "Survey About Nothing" monitors 1×10^6 red supergiants with the Large Binocular Telescope looking for the abrupt disappearance of any of these stars. In addition to potentially capturing a core-collapse failure, this survey could also detect VLE SNe coming from one of these sources. They would be visible as a sudden brightening of the "star" for of order a year, followed by a gradual but complete disappearance. After 7 years of observations Gerke *et al.* (2015) reviewed the survey data searching for both complete failures as well as the neutrino-mediated transients created by the Nadyozhin-Lovegrove effect as discussed in Chapter 2. Four candidates were initially recovered, but followup observations ruled out three sources as they later reappeared. The final candidate event satisfies the criteria for a very low energy supernova and will continue to be observed.

Reynolds *et al.* (2015) conducted a search through HST archival data looking for collapse events that were not flagged by survey selection rules at the time and recovered one candidate in the range 25 - 35 $M_{\odot}$that may have undergone an optically dark collapse.

5.3.1 Luminous Red Novae

Luminous red novae (LRNe) are observed transients too bright to be ordinary classical novae, but too faint and red to be supernovae. Although V838 Mon is now suspected to be a stellar merger event (Tylenda *et al.*, 2011), mergers and VLE SNe can have similar end results: a massive hydrogen envelope ejected at low energies. Spectroscopic observations show that most LRNe have dispersion velocities significantly higher than calculated for the neutrino-mediated transients. The observation of further transients may decide this question, or a search for remnants: the shedding of a common envelope by a binary merger will leave behind a degenerate remnant, but a failed CCSN will leave a black hole.

5.4 Candidate Shock Breakout Events

Several candidate shock breakout events have been published in the literature, but most are high-energy events suspected to come from compact progenitors. X-ray breakout bursts are slightly easier to detect because of the large number of existing space-based X-ray transient satellites designed specifically for the wide-field coverage and rapid slew time needed to capture breakout. In 2008 Soderberg *et al.* (2008) serendipitously captured an X-ray transient when a supernova went off during a Swift observation of its host galaxy. Soderberg *et al.* (2008) attribute this event to a Type Ib/c CCSN breaking out from a dense stellar wind surrounding its progenitor, a scenario consistent with the high mass loss rates of Type Ib/c progenitors near the end of their lives.[1] Unfortunately this rapid high-energy event, while of great interest on its own and as a proof of concept for shock breakout observations, bears little relation to the transients explored in this work. Closer to the VLE

[1] Modjaz *et al.* (2009) disagrees with Soderberg *et al.* (2008)'s analysis on several points. But both authors agree that the breakout originated in a compact progenitor, making it quite different from the breakouts studied here.

SNe regime, UV observations using the GALEX satellite in 2008 detected two CCSNe very close to the time of explosion: one with fading and one with rapidly rising UV emission, suggesting that the latter had been caught during its breakout phase (Gezari *et al.*, 2008). KEPLER hydrodynamic models combined with the CMFGEN radiation transport code were used to model the observed UV light curves as breakout in a 15 $M_{\odot}$ red supergiant exploding with a final kinetic energy 1.2 B and observed effective temperatures corresponding to breakouts similar to the high-energy end of the RSG15 models simulated in Chapter 4. The authors note an effect that will also come into play in the case of VLE SNe, namely that as the light curve fades the spectral temperature will also decline, which will bring more of the bolometric luminosity into the UV (or optical) observing window; the net effect being an apparent plateau phase that is actually the combination of these two factors.

5.4.1 Kepler Satellite Observations

In early 2016 Garnavich *et al.* (2016) announced the observation of two CCSNe with the Kepler satellite[2] and provided data suggesting the telescope had also captured the associated shock breakouts. The imaging cadence of Kepler is still insufficient to resolve the breakout itself, but subtracting models of the expected lightcurve from the data shows a systematic excess consistent with a breakout event producing additional luminosity at the beginning of the transient.

5.5 Current & Upcoming Observing Programs

The key to capturing these breakouts is high survey cadence, preferably hourly. Even a daily measurement can miss the more energetic breakouts entirely. In this area space-based observatories have an edge, but a global ground-based network could also achieve this frequency. LCOGT,

[2] Not to be confused with the KEPLER stellar evolution code.

which strives for at least one telescope in the dark at all times, has the best chance of reaching the necessary cadence from the ground. LSST's reasonably high cadence plus large collecting area would be excellent, but that must wait until LSST itself is built. Several space-based observatories would be capable of making these observations. The Kepler satellite was built for exoplanet detection, but when a malfunctioning reaction wheel recently rendered the telescope unable to maintain pointing to the precision necessary for its primary objective, it was repurposed through the Kepler-2 program for general wide-field studies. Kepler was originally designed to search for transiting exoplanets and was therefore built to detect small fluctuations in brightness over a wide field of view with a much higher cadence; this makes Kepler-2 more suited than most supernova searches to observe shock breakout. The TESS (Transiting Exoplanet Survey Satellite) mission will launch an instrument with similar capabilities to Kepler that would also be well-suited to detecting VLE SNe breakout. Many other planned missions could take good observations of breakout transients. The WFIRST mission would provide wide-field observations in the near-IR and the ULTRASAT program currently in design would launch a rapid-cadence UV satellite that would be ideal for detecting shock breakouts.

Followup in general should be simpler than for compact star breakouts since observers will have a response window measured in hours rather than seconds. HST's UVIS instrument can access the best wavelengths for observing. On the other end of the spectrum, if the soft X-ray emission is not absorbed, Swift's BAT would provide good warning of a breakout and the NuSTAR mission could make good observations. XMM-Newton might be able to capture the high end of the spectrum; Chandra's wavelength range is too high to detect meaningful emission. Among ground-based observatories, Pan-STARRS, PTF/ZTF, LCOGT, and eventually LSST could all make useful observations. The massive collecting areas of TMT and JWST could make excellent followup observations on these faint events even at optical and IR wavelengths.

Spectroscopic followup is strongly recommended to measure T_c. The spectrum of a red supergiant breakout will be dominated by the blackbody continuum and hydrogen-helium lines. It may also show absorption features from the surrounding nebula. Unlike the later supernova light curve, the breakout will show little to no nickel or iron emission. As the breakout proper fades and the envelope itself begins to move, the spectrum will relax back to a blackbody at the plateau effective temperature and the light curve will transition to photometric and spectroscopic behavior typical of a normal Type II SN.

5.6 Conclusions

VLE SNe breakout is expected to produce a blue ($> 1\times10^4$ K) transient with an approximate duration 3 - 70 h and a bolometric luminosity $10^{39}-10^{44}$ erg, with a reasonable fraction of this energy emitted at optical and IR wavelengths. The effects of color temperature on breakout luminosity at different frequencies are considered; they will act to further increase the brightness of VLE SNe at optical and IR wavelengths. Current and upcoming observation programs are assessed for suitability in detecting VLE SNe breakout. Cadence is the limiting factor for both existing and future surveys; breakout observations require cadence less than a day and preferably hourly. The best existing missions for detecting these events are wide-field transiting exoplanet searches.

Chapter 6

Further Work in VLE SNe Modeling

6.1 Models of Secondary Collisional Transients

Transients occurring before the actual core collapse of a massive star can cause it to shed a large quantity of mass in a short period of time. If multiple episodes of such mass loss occur, or if one of these shells is still close to the star when it explodes via core collapse, large quantities of mass can collide and produce highly luminous transients even if the original supernova was dim. The most well-known example of such transients is the pulsational-pair instability mechanism, but all that is required for such an event is that two mass shells carrying an appreciable amount of energy collide at a radius $r \sim 1 \times 10^{15}$ cm.[1] While pulsational-pair transients and low-mass transients may launch shells in completely different ways, if these shells collide with significant energy they will produce similar transients via similar interactions. Some stars at the low end of the CCSN progenitor mass range, generally 9 - 11 $M_{\odot}$, can undergo multiple violent burning stages that will also shed mass in shells (Woosley and Heger, 2015). A collision of these shells provides a way for VLE SNe to produce much brighter light curves than they otherwise would. Such an event may explain the unusual energy and morphology of the Crab Nebula, the remnant of SN1054. Supernovae exploding within dense mass loss will also show extensive interaction, and the class of Type IIn narrow-line supernovae suggest that at least some supernovae explode in dense environments.

6.2 The Curious Case of the Crab Nebula

Historical records of SN1054 suggest that it had a light curve with a peak luminosity roughly equivalent to a standard CCSN. But modern tallies of the amount of kinetic energy in the remnant produce a total closer to 0.5 B than 1.0B, and the observed nucleosynthesis is more compatible with a low-mass progenitor. The Crab Nebula also shows an unusual morphology; much of its mass is concentrated into a cold thin shell that also shows significant Rayleigh-Taylor instability, and there is no obvious expanding blastwave beyond this shell. These are the most obvious signatures of an unusual event; for a much more detailed discussion of all odd properties of the nebula and the explosion, see Smith (2013).

Both the unusual lightcurve and the unusual remnant can be explained by invoking a collision. The original low-energy event, possibly an electron-capture supernova, produced similarly low-energy ejecta, but a large fraction of the ejecta's kinetic energy was later converted into radiation and emitted. This produces both an anomalously bright light curve and anomalously slow ejecta, likely compacted into a thin cold shell at the collision interface. There are different models for the exact nature of this collision. Smith (2013) proposes a model in which the Crab supernova interacts with dense circumstellar medium. Yang and Chevalier (2015) argues against this particular model by noting that circumstellar interaction would create a velocity cutoff inconsistent with ob-

[1] If the collision occurs at a significantly smaller radius, the shells will be optically thick; if it occurs at a larger one, it will produce a radio transient instead.

servations; this does not, however, apply to a model where the ejecta collides with previously-shed mass from the star itself. Moriya *et al.* (2014) considers the general case of an electron capture supernova exploding inside a dense wind and finds it a viable model for the Crab. This study considers the specific case of presupernova explosive mass loss creating dense shells.

Woosley and Heger (2015) produces at least one low-mass progenitor with the appropriate mass-loss history. The 10 $M_{\odot}$star loses a dense shell of material to runaway Si burning approximately a year before collapse, then undergoes an electron-capture supernova. The ejecta from this explosion collides with the previously-shed material at $r \sim 1 \times 10^{15}$ cm. The kinetic energy and luminosity carried by these shells is sufficient to produce a lightcurve resembling a typical IIp, and approximate calculations suggest the transient should release the correct luminosity and result in ejecta of roughly the correct velocity. However, there is a major difference between simulating such an event in 1D and simulating it in two or three dimensions. Thin shells that are stable in 1D may become fragmented by instabilities. A true test of this model requires using the 10 $M_{\odot}$ model of Woosley and Heger (2015) as the initial condition for a 2D or 3D simulation of the collision in order to observe the formation of the shell and the possible effects of instabilities on luminosity.

Chapter 7

Conclusions: The Potential of VLE SNe

Observations - or null detections - of VLE SNe are key to understanding the full range of CCSNe outcomes and placing realistic, observationally-motived constraints on the failure and partial failure rate of supernovae. Even a star in which a standard core collapse explosion fails completely can still generate observable transients at or before its death. The mass lost to neutrinos during neutron star formation results, in some cases, in a shock sufficient to unbind the hydrogen envelope. The amount and history of the neutrino mass loss has a strong effect on the magnitude of the shock produced, as does the structure of the carbon-oxygen and helium cores of the progenitor star. In the two red supergiant models tested, the shock reached the base of the hydrogen envelope in a majority of the models with enough energy to eject it. These unusual transients will appear as low-energy, long-duration, red events as the ejected envelope emits its energy via hydrogen recombination. The ejected envelope has a speed on the order of 50 - 100 km/s and maintains a luminosity $10^{39} - 10^{40}$ ergs/s for approximately a year.

The shock breakout of SN1987A was modeled first as a test of the CASTRO multigroup radiation transport module and produced peak luminosities, durations, and color temperatures comparable to other published SN1987A breakout results. The spectral temperature behavior in this model motivates a discussion of the relative importance of opacity and of certain terms in the radiation transport equations. Opacity is considered both in the general case of shock breakout and in the specific case of low-energy events.. A range of VLE SNe were then modeled in two red supergiants, RSG15 and RSG25, bracketing the suspected mass range of failed supernovae. These events give light curves and spectra that show clear variations with both explosion energy and progenitor radius. Analytic solutions tested against these numerical results provide reasonable approximations of the results.

Supernova shock breakout represents a promising method for both detecting otherwise dim supernova and retrieving information about their progenitor stars. Shock breakouts in VLE SNe in particular are easier to observe than those in regular CCSNe because of their extended duration, and are easier to observe than their associated SN because of their higher luminosity. In red supergiants the effective temperature of the breakout places the bulk of the emission in the hard UV bands rather than the X-ray, making them easier to observe with existing instruments.

Very-low-energy supernovae are both an interesting subset of supernova explosions in and of themselves and a promising means of studying core-collapse supernovae from a new angle.

Bibliography

Akmal, A.; Pandharipande, V. R. and Ravenhall, D. G. Equation of state of nucleon matter and neutron star structure. Phys. Rev. C **58**, 1804 (1998).

Almgren, A. S.; Beckner, V. E.; Bell, J. B.; Day, M. S.; Howell, L. H.; Joggerst, C. C.; Lijewski, M. J.; Nonaka, A.; Singer, M. and Zingale, M. CASTRO: A New Compressible Astrophysical Solver. I. Hydrodynamics and Self-gravity. ApJ **715**, 1221 (2010).

Arnett, W. D.; Bahcall, J. N.; Kirshner, R. P. and Woosley, S. E. Supernova 1987A. ARA&A **27**, 629 (1989).

Brezzi, F.; Lipnikov, K.; Shashkov, M. and Simoncini, V. A new discretization methodology for diffusion problems on generalized polyhedral meshes. *Computer Methods in Applied Mechanics and Engineering* **196**, 3682 (2007). Special Issue Honoring the 80th Birthday of Professor Ivo Babu.

Brezzi, F.; Lipnikov, K. and Simoncini, V. A family of mimetic finite difference methods on polygonal and polyhedral meshes. *Mathematical Methods and Methods in Applied Sciences* **15**, 1533–1551 (2005).

Brown, J. M. and Woosley, S. E. Nucleosynthetic Constraints on the Mass of the Heaviest Supernovae. ApJ **769**, 99 (2013a).

Brown, J. M. and Woosley, S. E. Nucleosynthetic Constraints on the Mass of the Heaviest Supernovae. ApJ **769**, 99 (2013b).

Buchler, J. R. Radiation transfer in the fluid frame. *Journal of Quantitative Spectroscopy and Radiative Transfer* **30**, 395 (1983).

Burrows, A. Supernova neutrinos. ApJ **334**, 891 (1988).

Burrows, A. and Lattimer, J. M. Neutrinos from SN 1987A. ApJ **318**, L63 (1987).

Burton, D. E. Connectivity structures and differencing techniques for staggered-grid free-Lagrange hydrodynamics. In Shih, H. J.; Schiesser, W. and Ellison, J., eds., *Presented at the 7th International Association of Mathematics and Computer Simulation (IMACS) International Conference on Computer Methods for Partial Differential Equations, New Brunswick, NJ, 22-24 Jun. 1992* (1992), vol. UCRL-JC-110555, pp. 22–24.

Castor, J. *Radiation Hydrodynamics*. Cambridge University Press (2004).

Clausen, D.; Piro, A. L. and Ott, C. D. The Black Hole Formation Probability. ApJ **799**, 190 (2015).

Demorest, P. B.; Pennucci, T.; Ransom, S. M.; Roberts, M. S. E. and Hessels, J. W. T. A two-solar-mass neutron star measured using Shapiro delay. Nature **467**, 1081 (2010).

Ensman, L. and Burrows, A. Shock breakout in SN 1987A. ApJ **393**, 742 (1992).

Fransson, C.; Cassatella, A.; Gilmozzi, R.; Kirshner, R. P.; Panagia, N.; Sonneborn, G. and

Wamsteker, W. Narrow ultraviolet emission lines from SN 1987A - Evidence for CNO processing in the progenitor. ApJ **336**, 429 (1989).

Garnavich, P. M.; Tucker, B. E.; Rest, A.; Shaya, E. J.; Olling, R. P.; Kasen, D. and Villar, A. Shock Breakout and Early Light Curves of Type II-P Supernovae Observed with Kepler. ApJ **820**, 23 (2016).

Gerke, J. R.; Kochanek, C. S. and Stanek, K. Z. The search for failed supernovae with the Large Binocular Telescope: first candidates. MNRAS **450**, 3289 (2015).

Gezari, S.; Dessart, L.; Basa, S.; Martin, D. C.; Neill, J. D.; Woosley, S. E.; Hillier, D. J.; Bazin, G.; Forster, K.; Friedman, P. G.; Le Du, J.; Mazure, A.; Morrissey, P.; Neff, S. G.; Schiminovich, D. and Wyder, T. K. Probing Shock Breakout with Serendipitous GALEX Detections of Two SNLS Type II-P Supernovae. ApJ **683**, L131 (2008).

Gustafsson, B.; Edvardsson, B.; Eriksson, K.; Jï£¡rgensen, U. G.; Nordlund, ï£¡. and Plez, B. A grid of marcs model atmospheres for late-type stars. A&A **486**, 951 (2008).

Horiuchi, S.; Beacom, J. F.; Kochanek, C. S.; Prieto, J. L.; Stanek, K. Z. and Thompson, T. A. The Cosmic Core-collapse Supernova Rate Does Not Match the Massive-star Formation Rate. ApJ **738**, 154 (2011).

Hyman, J.; Shashkov, M. and Steinberg, S. The numerical solution of diffusion problems in strongly heterogeneous non-isotropic materials. *Journal of Computational Physics* **132**, 130 (1997).

Kasen, D. and Woosley, S. E. Type II Supernovae: Model Light Curves and Standard Candle Relationships. ApJ **703**, 2205 (2009).

Kasen, D.; Woosley, S. E. and Heger, A. Pair Instability Supernovae: Light Curves, Spectra, and Shock Breakout. ApJ **734**, 102 (2011).

Katz, B.; Budnik, R. and Waxman, E. Fast radiation mediated shocks and supernova shock breakouts. ApJ **716**, 781 (2010).

Klein, R. I. and Chevalier, R. A. X-ray bursts from Type II supernovae. ApJ **223**, L109 (1978).

Kochanek, C. S. Failed Supernovae Explain the Compact Remnant Mass Function. ApJ **785**, 28 (2014).

Kochanek, C. S.; Beacom, J. F.; Kistler, M. D.; Prieto, J. L.; Stanek, K. Z.; Thompson, T. A. and Yüksel, H. A Survey About Nothing: Monitoring a Million Supergiants for Failed Supernovae. ApJ **684**, 1336 (2008).

Krumholz, M. R.; Klein, R. I.; McKee, C. F. and Bolstad, J. Equations and Algorithms for Mixed-frame Flux-limited Diffusion Radiation Hydrodynamics. ApJ **667**, 626 (2007).

Lattimer, J. M. and Prakash, M. Neutron Star Structure and the Equation of State. ApJ **550**, 426 (2001).

Lattimer, J. M. and Yahil, A. Analysis of the neutrino events from supernova 1987A. ApJ **340**, 426 (1989).

Levermore, C. D. Relating Eddington factors to flux limiters. *Journal of Quantitative Spectroscopy and Radiative Transfer* **31**, 149 (1984).

Levermore, C. D. and Pomraning, G. C. A flux-limited diffusion theory. ApJ **248**, 321 (1981a).

Levermore, C. D. and Pomraning, G. C. A flux-limited diffusion theory. *Astrophysical Journal* **248**, 321 (1981b).

Li, X.-D. A Fallback Disk Model for Ultraluminous X-Ray Sources. ApJ **596**, L199 (2003).

Lovegrove, E. and Woosley, S. E. Very Low Energy Supernovae from Neutrino Mass Loss. ApJ **769**, 109 (2013).

Lundqvist, P. and Fransson, C. The Line Emission from the Circumstellar Gas around SN 1987A. ApJ **464**, 924 (1996).

MacFadyen, A. I. and Woosley, S. E. Collapsars: Gamma-Ray Bursts and Explosions in "Failed Supernovae". ApJ **524**, 262 (1999).

MacFadyen, A. I.; Woosley, S. E. and Heger, A. Supernovae, Jets, and Collapsars. ApJ **550**, 410 (2001).

Matzner, C. D. and McKee, C. F. The Expulsion of Stellar Envelopes in Core-Collapse Supernovae. ApJ **510**, 379 (1999).

Modjaz, M.; Li, W.; Butler, N.; Chornock, R.; Perley, D.; Blondin, S.; Bloom, J. S.; Filippenko, A. V.; Kirshner, R. P.; Kocevski, D.; Poznanski, D.; Hicken, M.; Foley, R. J.; Stringfellow, G. S.; Berlind, P.; Barrado y Navascues, D.; Blake, C. H.; Bouy, H.; Brown, W. R.; Challis, P.; Chen, H.; de Vries, W. H.; Dufour, P.; Falco, E.; Friedman, A.; Ganeshalingam, M.; Garnavich, P.; Holden, B.; Illingworth, G.; Lee, N.; Liebert, J.; Marion, G. H.; Olivier, S. S.; Prochaska, J. X.; Silverman, J. M.; Smith, N.; Starr, D.; Steele, T. N.; Stockton, A.; Williams, G. G. and Wood-Vasey, W. M. From Shock Breakout to Peak and Beyond: Extensive Panchromatic Observations of the Type Ib Supernova 2008D Associated with Swift X-ray Transient 080109. ApJ **702**, 226 (2009).

Morel, J. Lagrangian solution of the radiation-hydrodynamics equations with grey radiation diffusion (????). Unpublished lecture notes.

Moriya, T. J.; Tominaga, N.; Langer, N.; Nomoto, K.; Blinnikov, S. I. and Sorokina, E. I. Electron-capture supernovae exploding within their progenitor wind. A&A **569**, A57 (2014).

Munari, U.; Henden, A.; Kiyota, S.; Laney, D.; Marang, F.; Zwitter, T.; Corradi, R. L. M.; Desidera, S.; Marrese, P. M.; Giro, E.; Boschi, F. and Schwartz, M. B. The mysterious eruption of V838 Mon. A&A **389**, L51 (2002).

Nadezhin, D. K. Some secondary indications of gravitational collapse. Ap&SS **69**, 115 (1980).

Nakar, E. and Sari, R. Early Supernovae Light Curves Following the Shock Breakout. ApJ **725**, 904 (2010).

O'Connor, E. and Ott, C. D. Black Hole Formation in Failing Core-Collapse Supernovae. ApJ **730**, 70 (2011).

Oppenheimer, J. R. and Volkoff, G. M. On Massive Neutron Cores. *Physical Review* **55**, 374 (1939).

Pejcha, O. and Thompson, T. A. The Landscape of the Neutrino Mechanism of Core-collapse Supernovae: Neutron Star and Black Hole Mass Functions, Explosion Energies, and Nickel Yields. ApJ **801**, 90 (2015).

Piro, A. L. Taking the "Un" out of "Unnovae". ApJ **768**, L14 (2013).

Popov, D. V. An analytical model for the plateau stage of Type II supernovae. ApJ **414**, 712 (1993).

Prakash, M.; Bombaci, I.; Prakash, M.; Ellis, P. J.; Lattimer, J. M. and Knorren, R. Composition and structure of protoneutron stars. Phys. Rep. **280**, 1 (1997).

Quataert, E. and Shiode, J. Wave-driven mass loss in the last year of stellar evolution: setting the stage for the most luminous core-collapse supernovae. MNRAS **423**, L92 (2012a).

Quataert, E. and Shiode, J. Wave-driven mass loss in the last year of stellar evolution: setting the stage for the most luminous core-collapse supernovae. MNRAS **423**, L92 (2012b).

Rabinak, I. and Waxman, E. The Early UV/Optical Emission from Core-collapse Supernovae. ApJ **728**, 63 (2011).

Reynolds, T. M.; Fraser, M. and Gilmore, G. Gone without a bang: an archival HST survey for disappearing massive stars. MNRAS **453**, 2885 (2015).

Shashkov, M. and Steinberg, S. Solving diffusion equations with rough coefficients in rough grids. *Journal of Computational Physics* **129**, 383 (1996).

Shewchuk, J. R. An introduction to the conjugate gradient method without the agonizing pain. Tech. rep., Pittsburgh, PA, USA (1994).

Shiode, J. H. and Quataert, E. Setting the Stage for Circumstellar Interaction in Core-Collapse Supernovae. II. Wave-driven Mass Loss in Supernova Progenitors. ApJ **780**, 96 (2014).

Smartt, S. J. Observational Constraints on the Progenitors of Core-Collapse Supernovae: The Case for Missing High-Mass Stars. PASA **32**, e016 (2015).

Smith, N. The Crab nebula and the class of Type IIn-P supernovae caused by sub-energetic electron-capture explosions. MNRAS **434**, 102 (2013).

Smith, N.; Li, W.; Silverman, J. M.; Ganeshalingam, M. and Filippenko, A. V. Luminous blue variable eruptions and related transients: diversity of progenitors and outburst properties. *MNRAS* **415**, 773 (2011).

Soderberg, A. M.; Berger, E.; Page, K. L.; Schady, P.; Parrent, J.; Pooley, D.; Wang, X.-Y.; Ofek, E. O.; Cucchiara, A.; Rau, A.; Waxman, E.; Simon, J. D.; Bock, D. C.-J.; Milne, P. A.; Page, M. J.; Barentine, J. C.; Barthelmy, S. D.; Beardmore, A. P.; Bietenholz, M. F.; Brown, P.; Burrows, A.; Burrows, D. N.; Byrngelson, G.; Cenko, S. B.; Chandra, P.; Cummings, J. R.; Fox, D. B.; Gal-Yam, A.; Gehrels, N.; Immler, S.; Kasliwal, M.; Kong, A. K. H.; Krimm, H. A.; Kulkarni, S. R.; Maccarone, T. J.; Mészáros, P.; Nakar, E.; O'Brien, P. T.; Overzier, R. A.; de Pasquale, M.; Racusin, J.; Rea, N. and York, D. G. An extremely luminous X-ray outburst at the birth of a supernova. Nature **453**, 469 (2008).

Sukhbold, T.; Ertl, T.; Woosley, S. E.; Brown, J. M. and Janka, H.-T. Core-Collapse Supernovae from 9 to 120 Solar Masses Based on Neutrino-powered Explosions. *ArXiv e-prints* (2015).

Sukhbold, T. and Woosley, S. E. The Compactness of Presupernova Stellar Cores. ApJ **783**, 10 (2014).

Tolstov, A. G.; Blinnikov, S. I. and Nadyozhin, D. K. Coupling of matter and radiation at supernova shock breakout. MNRAS **429**, 3181 (2013).

Tominaga, N.; Morokuma, T.; Blinnikov, S. I.; Baklanov, P.; Sorokina, E. I. and Nomoto, K. Shock Breakout in Type II Plateau Supernovae: Prospects for High-Redshift Supernova Surveys. ApJS **193**, 20 (2011).

Turner, N. J. and Stone, J. M. A Module for Radiation Hydrodynamic Calculations with ZEUS-2D Using Flux-limited Diffusion. *The Astrophysical Journal Supplement Series* **135**, 95 (2001).

Tylenda, R.; Hajduk, M.; Kamiński, T.; Udalski, A.; Soszyński, I.; Szymański, M. K.; Kubiak, M.; Pietrzyński, G.; Poleski, R.; Wyrzykowski, Ł. and Ulaczyk, K. V1309 Scorpii: merger of a contact binary. A&A **528**, A114 (2011).

Ugliano, M.; Janka, H.-T.; Marek, A. and Arcones, A. Progenitor-explosion Connection and Remnant Birth Masses for Neutrino-driven Supernovae of Iron-core Progenitors. ApJ **757**, 69 (2012).

Weaver, T. A.; Zimmerman, G. B. and Woosley, S. E. Presupernova evolution of massive stars. ApJ **225**, 1021 (1978).

Whalen, D. J.; Even, W.; Frey, L. H.; Smidt, J.; Johnson, J. L.; Lovekin, C. C.; Fryer, C. L.; Stiavelli, M.; Holz, D. E.; Heger, A.; Woosley, S. E. and Hungerford, A. L. Finding the First Cosmic Explosions. I. Pair-instability Supernovae. ApJ **777**, 110 (2013).

Woosley, S. E. Gamma-ray bursts from stellar mass accretion disks around black holes. ApJ **405**, 273 (1993).

Woosley, S. E. and Heger, A. Nucleosynthesis and remnants in massive stars of solar metallicity. Phys. Rep. **442**, 269 (2007).

Woosley, S. E. and Heger, A. Long Gamma-Ray Transients from Collapsars. ApJ **752**, 32 (2012).

Woosley, S. E. and Heger, A. The Remarkable Deaths of 9-11 Solar Mass Stars. ApJ **810**, 34 (2015).

Woosley, S. E.; Heger, A. and Weaver, T. A. The evolution and explosion of massive stars. *Reviews of Modern Physics* **74**, 1015 (2002).

Yang, H. and Chevalier, R. A. Evolution of the Crab Nebula in a Low Energy Supernova. ApJ **806**, 153 (2015).

Zhang, W.; Howell, L.; Almgren, A.; Burrows, A. and Bell, J. CASTRO: A New Compressible Astrophysical Solver. II. Gray Radiation Hydrodynamics. ApJS **196**, 20 (2011).

Zhang, W.; Howell, L.; Almgren, A.; Burrows, A.; Dolence, J. and Bell, J. CASTRO: A New Compressible Astrophysical Solver. III. Multigroup Radiation Hydrodynamics. ApJS **204**, 7 (2013).